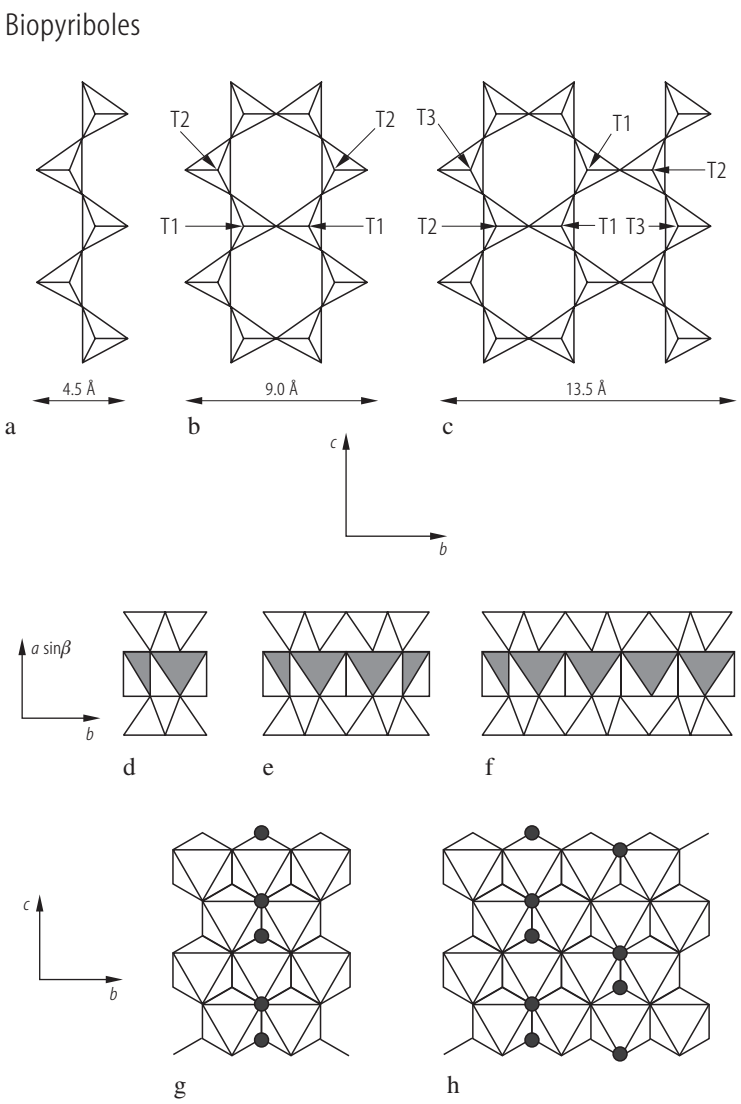

Fig. 1. Biopyriboles. Silicate chains formed by sharing SiO_4 tetrahedra. (**a**) Single-chain (pyroxenes), (**b**) double-chain (amphiboles), (**c**) triple-chain silicates. The chain widths indicated are 0.5 [010]. The tetrahedral sites are labeled using the next-nearest neighbour notation. (**d-f**) The interlayer octahedral ribbons corresponding to structures (**a-c**). Viewing direction is along the *c*-axis parallel to the elongation of the silicate chains. (**g, h**) Parts of the octahedral ribbons of the sodic amphibole and sodium-jimthompsonite (SJT), respectively, showing the normal distribution of OH sites (solid circles) in the two structures [92W1, 77V1].

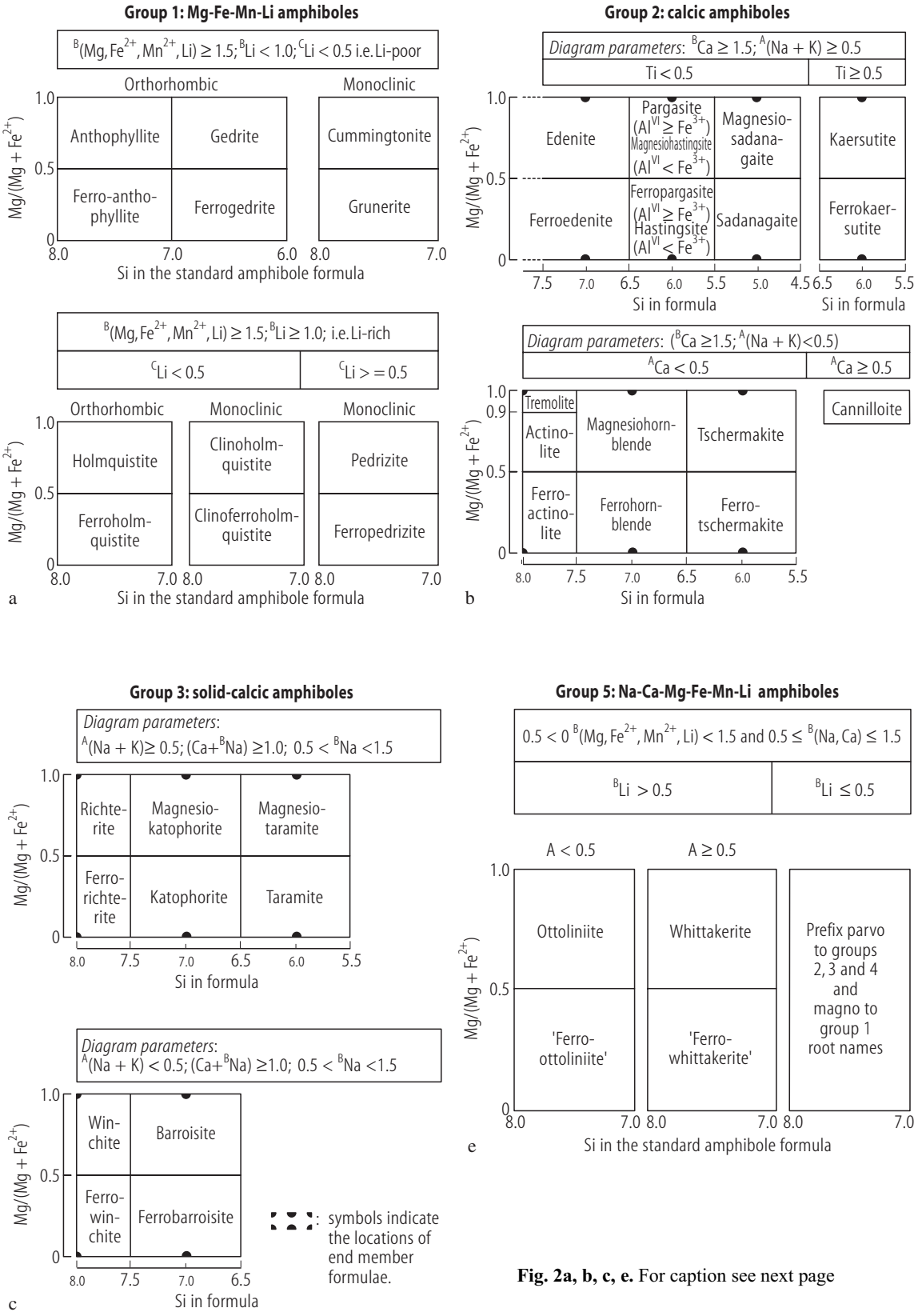

Fig. 2a, b, c, e. For caption see next page

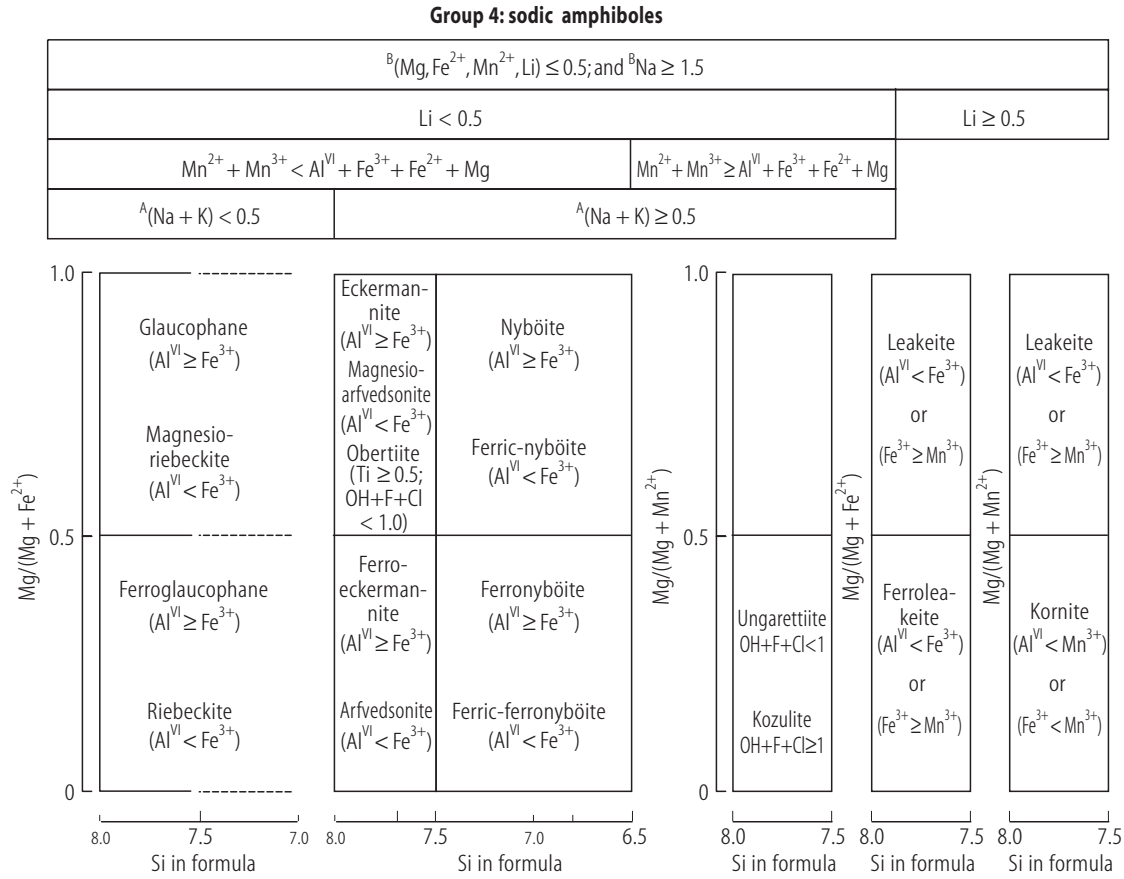

Fig. 2. The amphibole groups. (**a**) Mg-Fe-Mn-Li amphiboles; (**b**) calcic amphiboles; (**c**) sodic-calcic amphiboles; (**d**) sodic amphiboles; (**e**) Na-Ca-Mg-Fe-Mn-Li amphiboles [97L2, 04L1]. Final names require the relevant prefixes which are listed in Table 1b and may optionally include the modifiers that are found in Table 1c. - Symbols in (**b**) and (**c**) (semi-circles, quarter-circles) indicate the locations of end-member formulae.

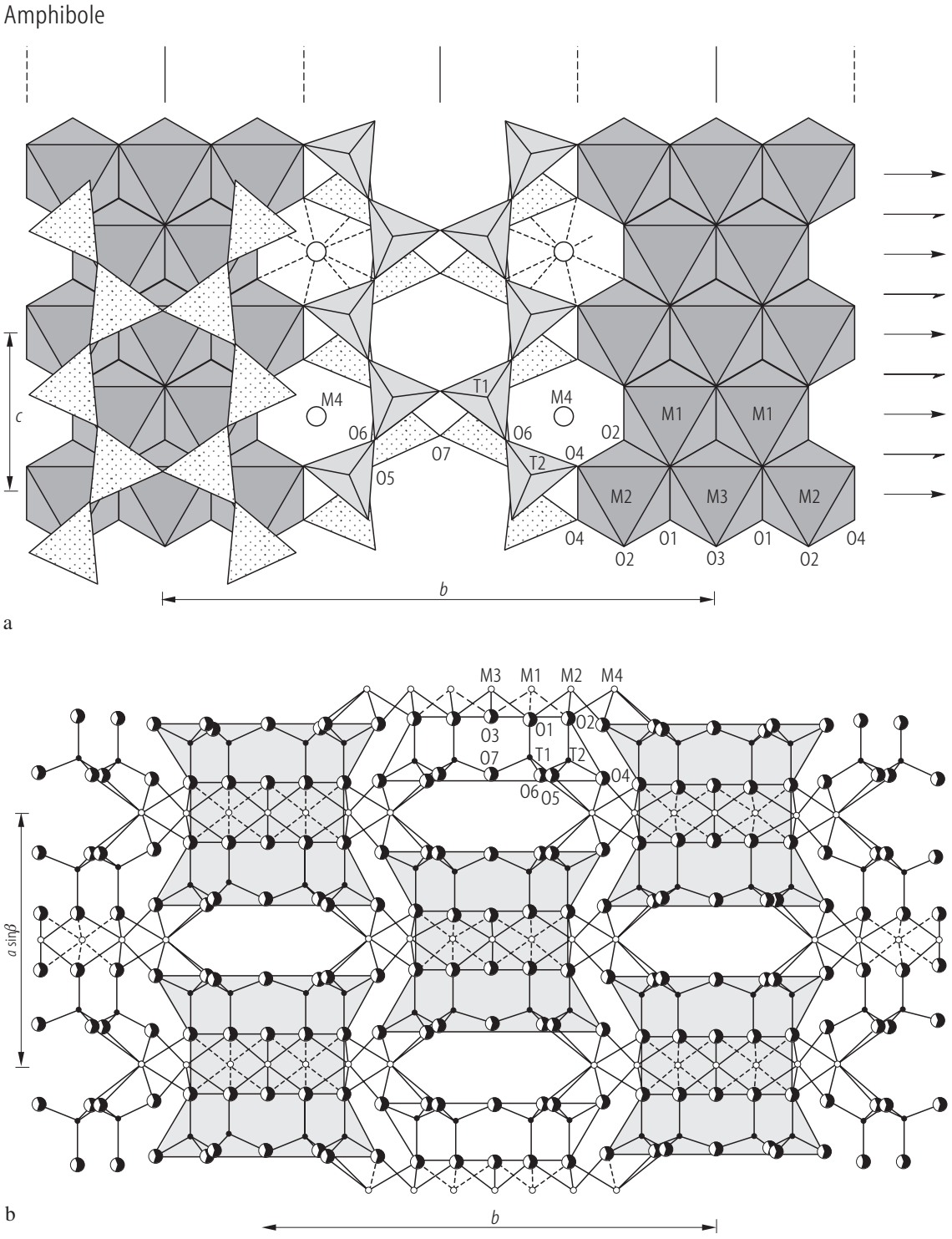

Fig. 3a, b. For caption see next page.

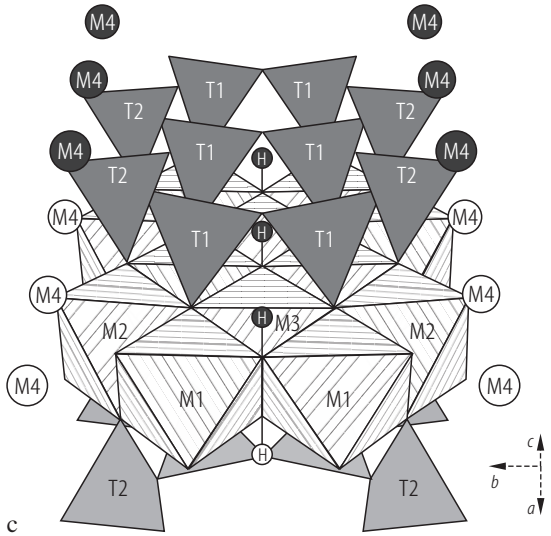

Fig. 3. Crystal structure of C2/m amphibole. (**a**) View along the [100] direction [83H1]; (**b**) crystal structure projected down [001] [79C1]. Stippled areas outline I-beams depicted in Fig. 4; (**c**) I-beam with surrounding M4 sites. A strip of edge-sharing octahedra is intercalated between two corner-sharing double tetrahedral chains in apex-to-apex arrangement. The M2 and M4 sites provide the linkages to adjacent I-beams [83H1, 03N1].

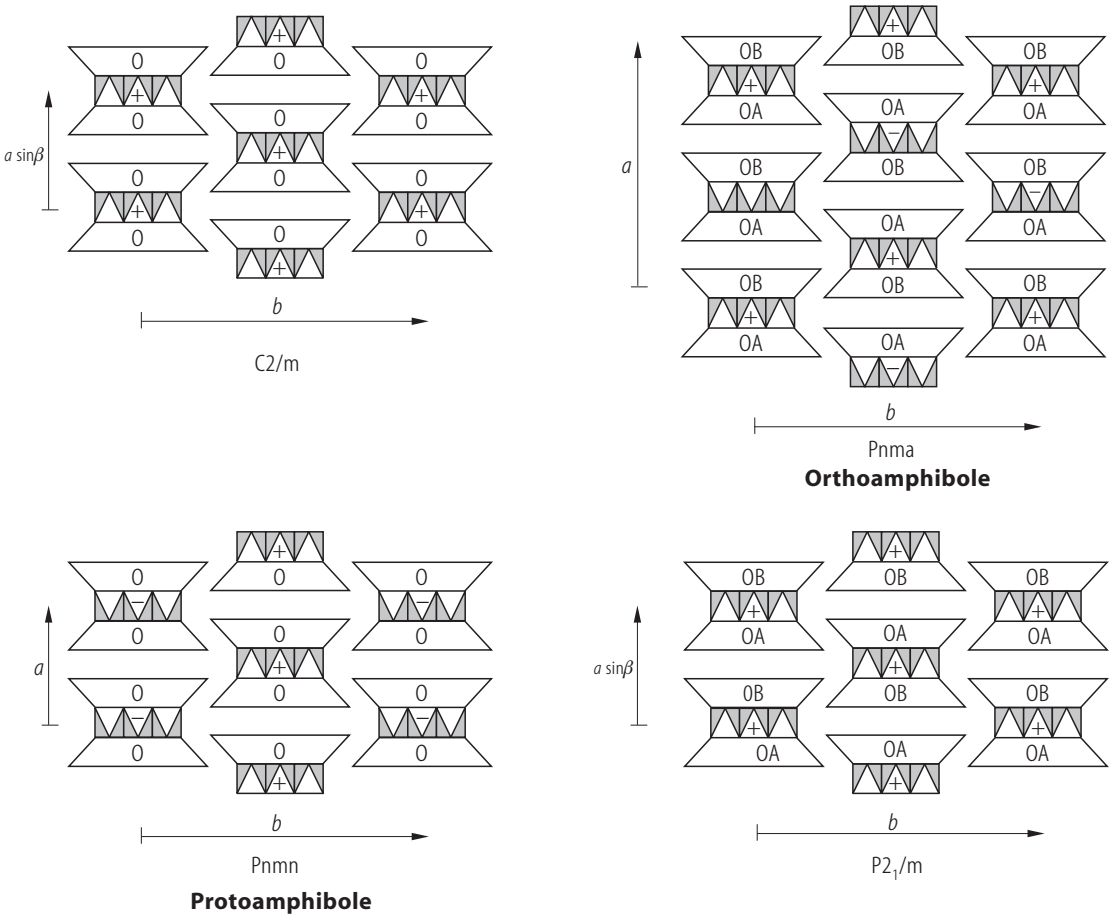

Fig. 4. Amphiboles. Structural topology [76P1].

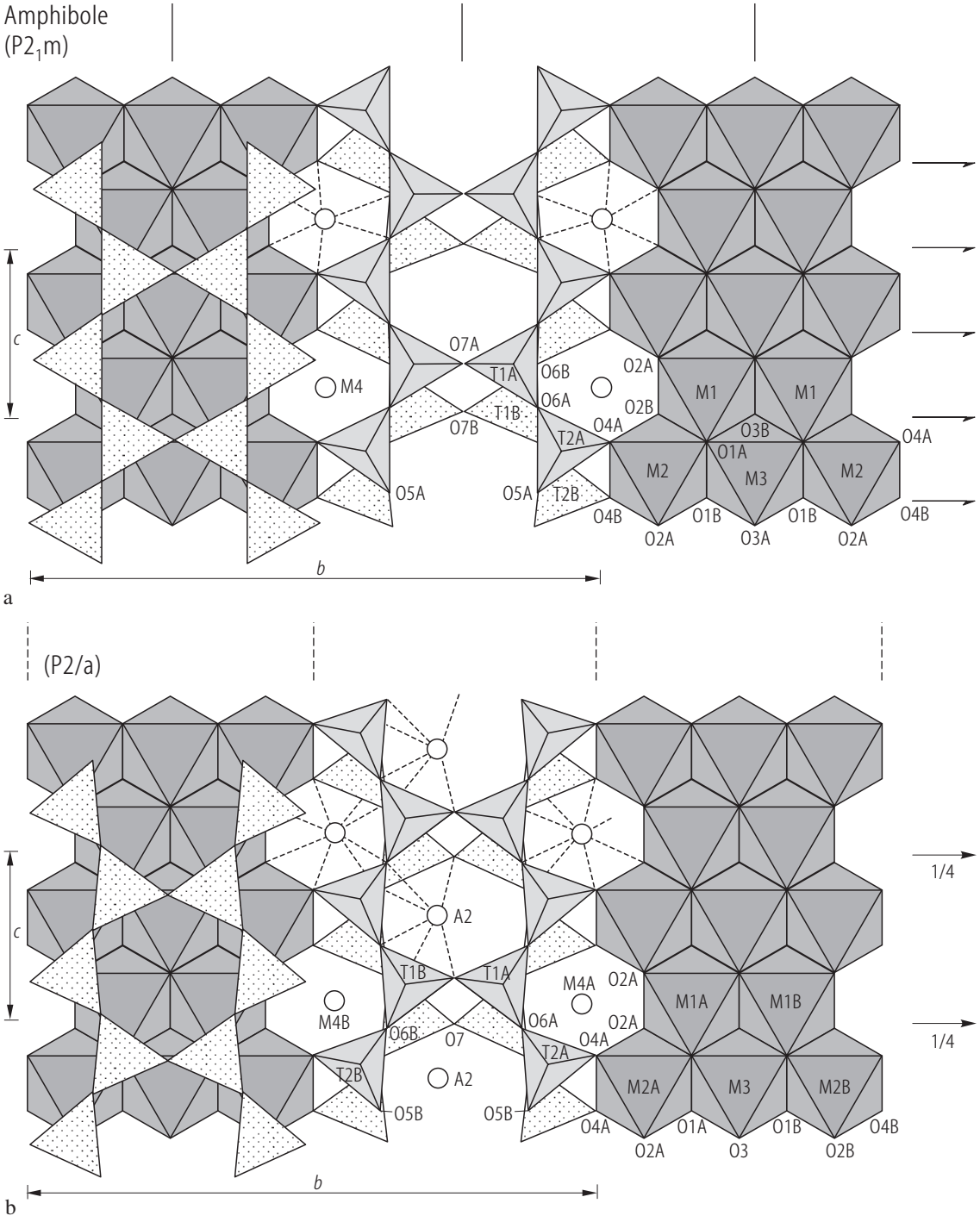

Fig. 5a,b. For caption see next page.

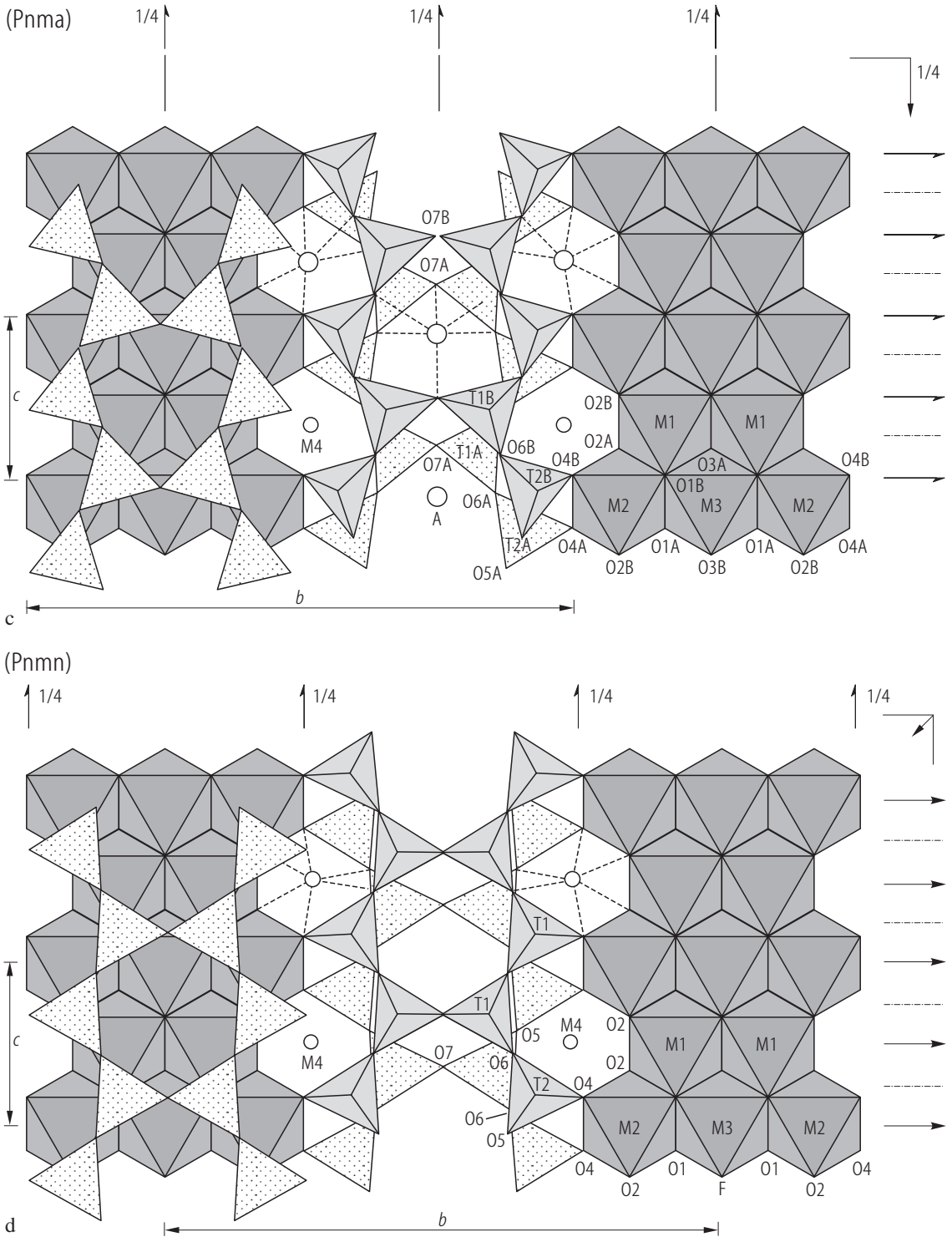

Fig. 5. Amphiboles. Crystal structures projected on the (100): **(a)** $P2_1/m$; **(b)** P2/a; **(c)** Pnma; **(d)** Pnmn. The space-group symmetry elements are also shown [83H1].

→

Fig. 8. Sodic ferripedrizite. Electron density distribution around (**a**) the M4 site (projected onto (100); contours at 1.0 $e/Å^3$; dots give positions of M4'(Li) and M4(Na)); (**b**) the A site (best plane passing through A and Am dots giving their positions; contours at 1.0 $e/Å^3$) [00O1].

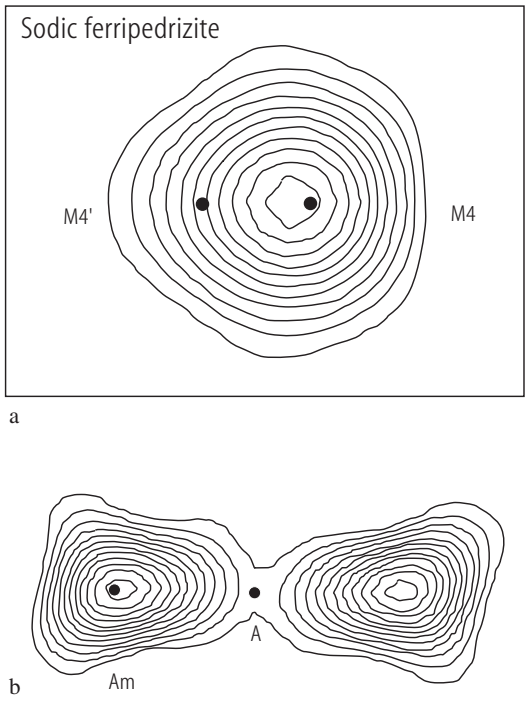

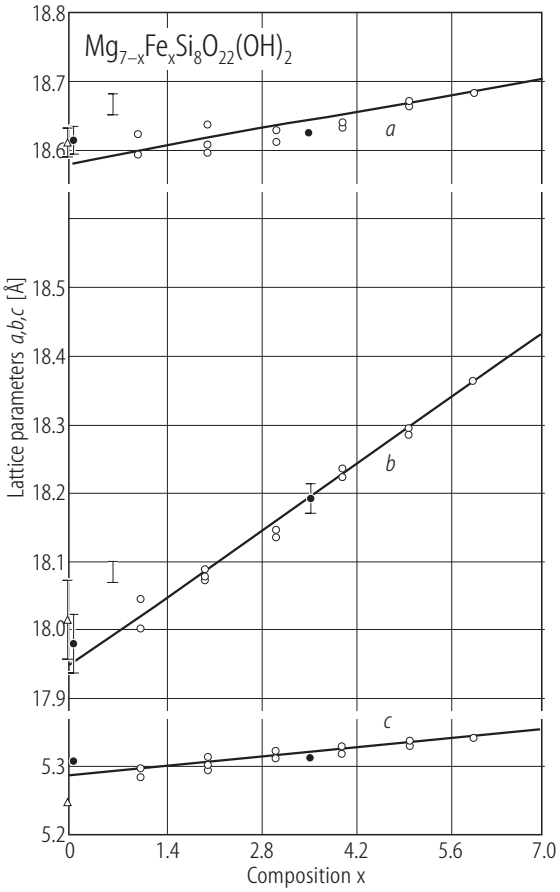

Fig. 6. $Mg_{7-x}Fe_xSi_8O_{22}(OH)_2$ orthorhombic amphiboles. Composition dependences of the lattice parameters: open circles [76P2]; triangles [63G1]; full circles [75C3].

For Fig. 7 see next page

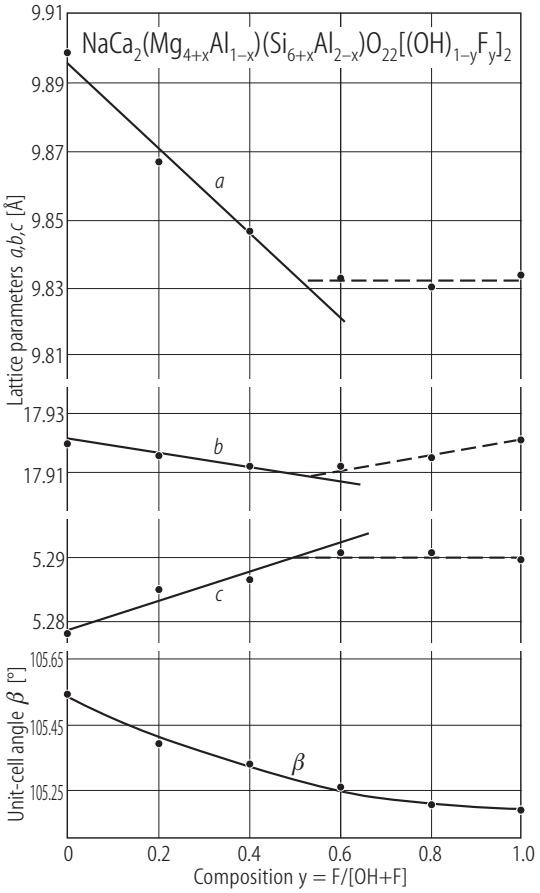

Fig. 9. $NaCa_2(Mg_{4+x}Al_{1-x})(Si_{6+x}Al_{2-x})O_{22}[(OH)_{1-y}F_y]_2$. Unit cell parameters along the join pargasite – fluoro-pargasite as function of F/(OH+F) [00R1]. The Al/(Al+Si) content was ≅ 0.32 for nominal y ≤ 0.6 and 0.29 for y ≥ 0.8.

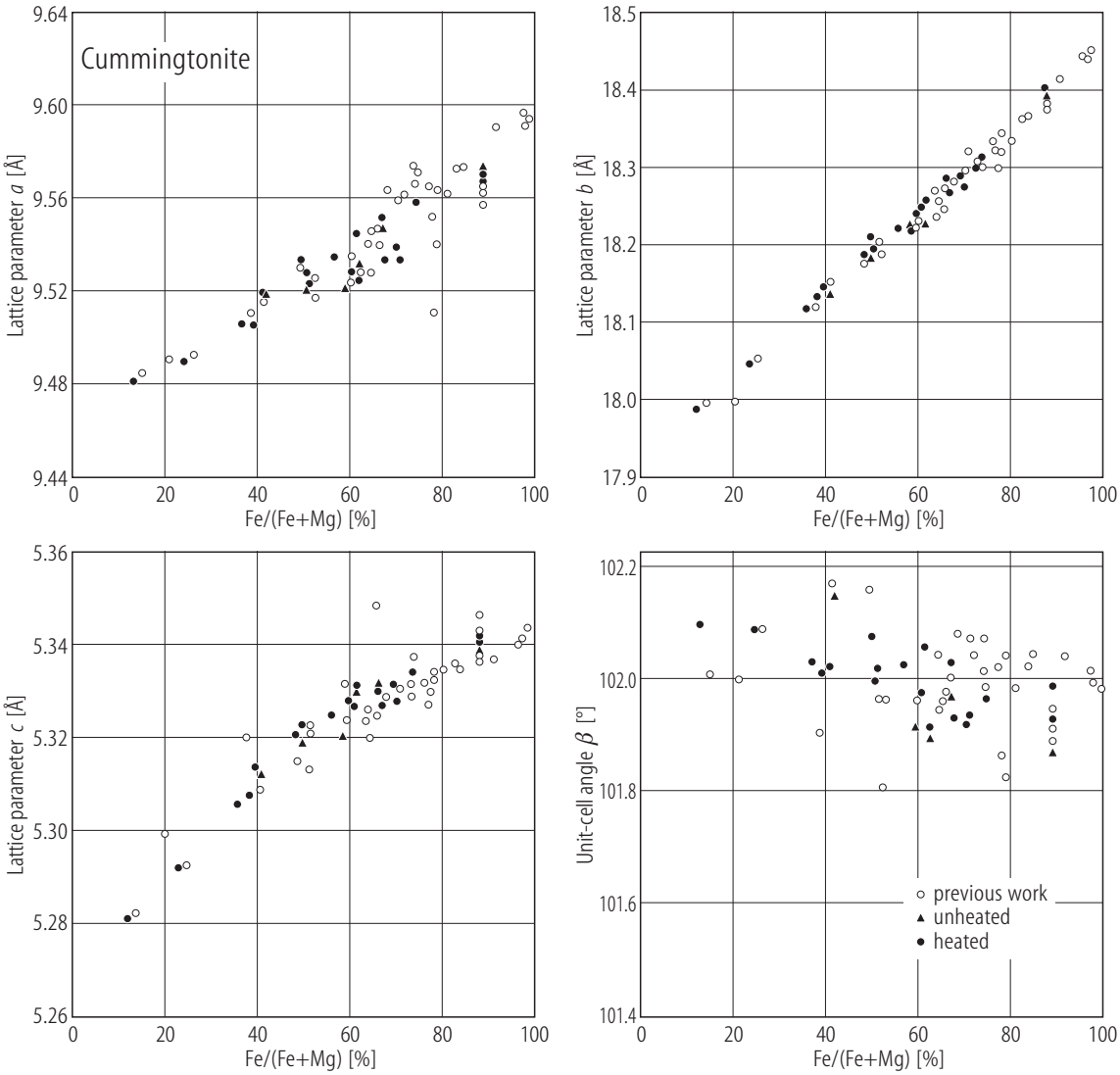

Fig. 7. Cummingtonite (natural and heated). Lattice parameters as function of iron content. Data for unheated and heated samples are from [94H2]. Data from previous work on natural cummingtonites are from [67K1, 69K1, 73K1, 74R1, 80H1, 88C1, 92L1, 92Z2].

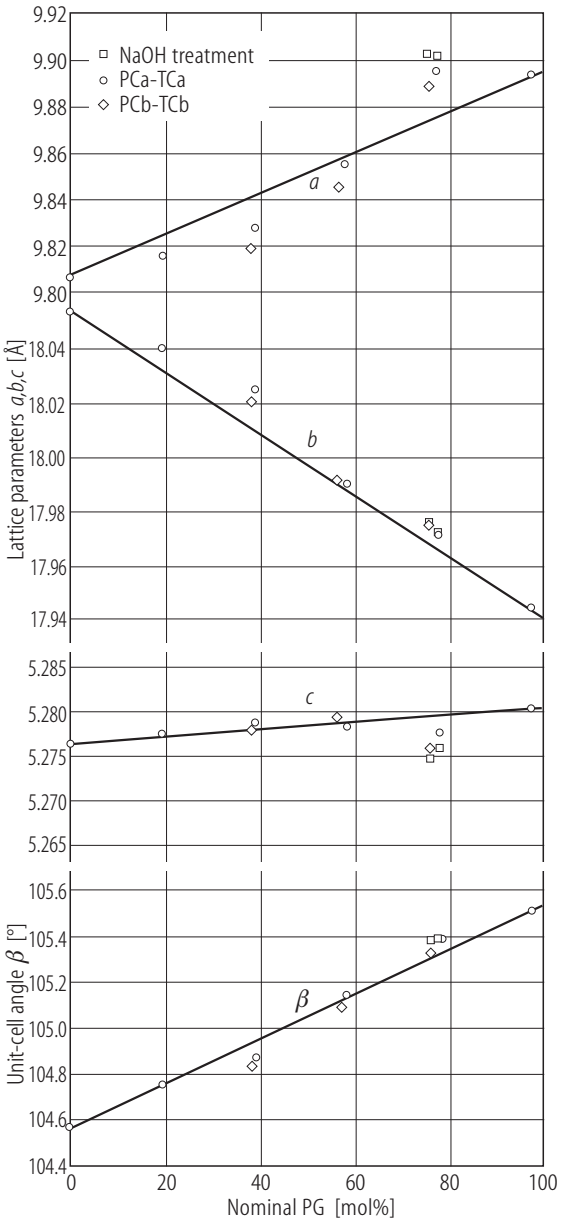

Fig. 10. $Na_{0.975}Ca_{1.95}Mg_{4.075}Al_{2.925}Si_{6.05}O_{22}(OH)_2$ (PCa) – $Ca_{1.8}Mg_{5.20}Si_8O_{22}(OH)_2$ (TCa) (circles) and $Na_{0.95}Ca_{1.90}Mg_{4.15}Al_{2.85}Si_{6.1}O_{22}(OH)_2$(PCb) – $Ca_{1.7}Mg_{5.3}Si_8O_{22}(OH)_2$ (TCb) (diamond). Composition dependences of lattice parameters. Squares indicate amphiboles formed in a 0.25m NaOH solution [99S1]. The straight lines are without significance. *x*-axis is nominal pargasite (PG).

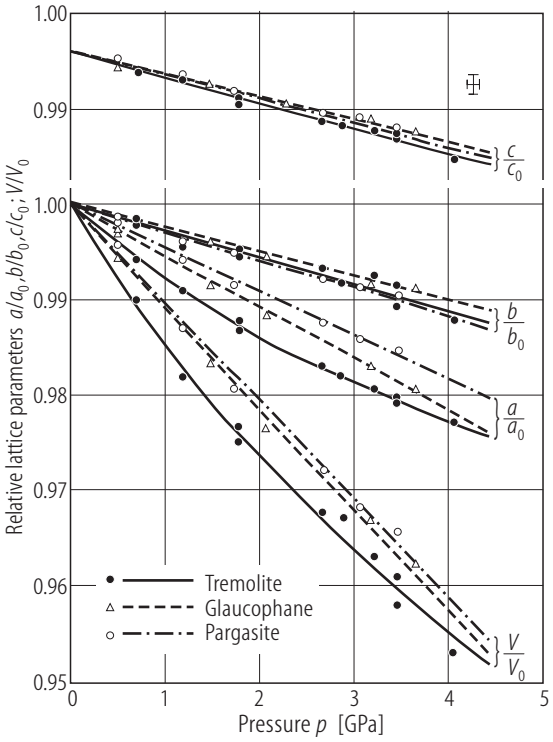

Fig. 11. Tremolite, glaucophane, pargasite. Cell volumes and lattice parameters as function of pressure [91C1]. The cross indicates the error bar. Lattice parameters and volume are normalized to the ambient pressure value.

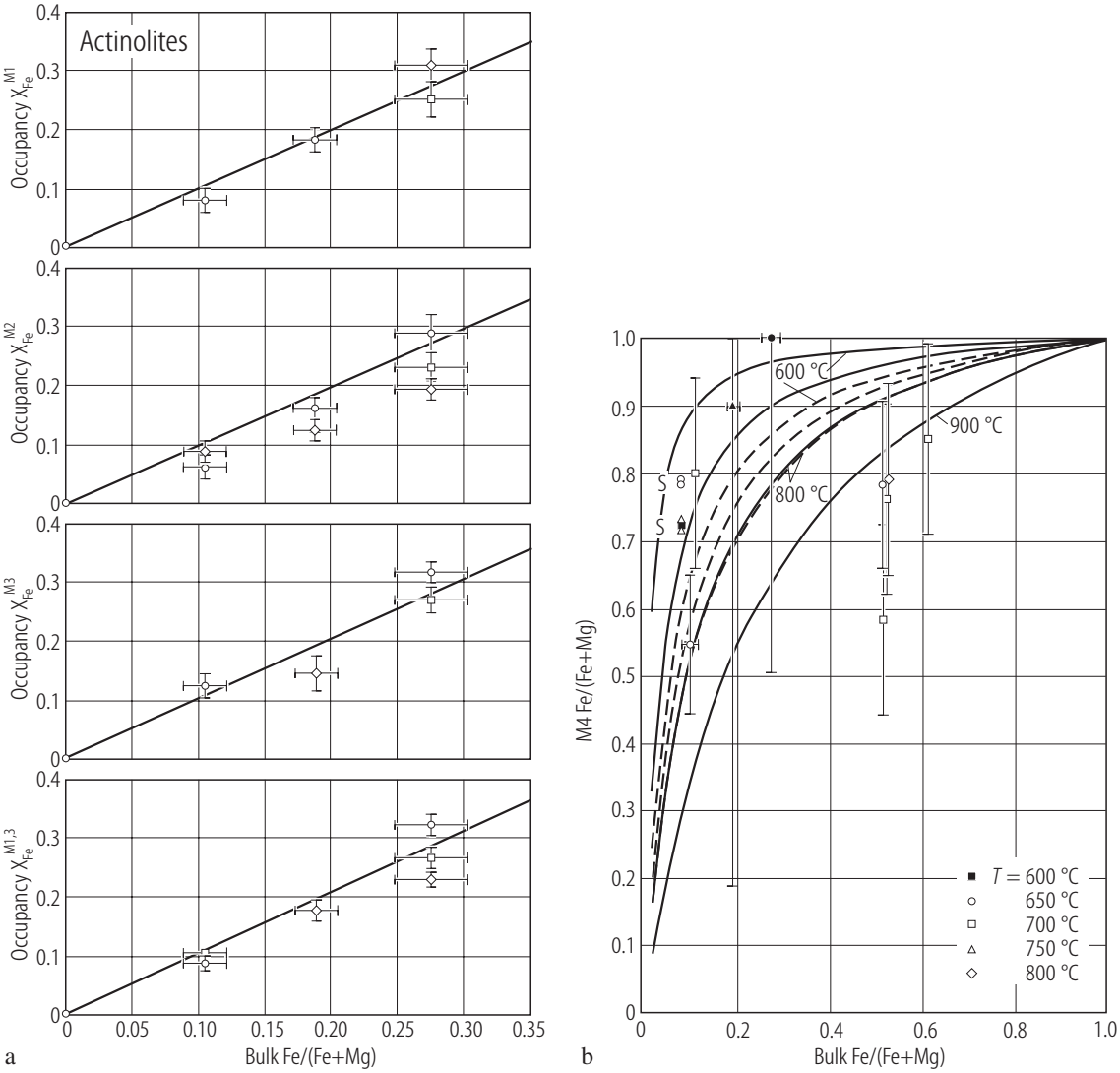

Fig. 12. Actinolites. (**a**) Plots of Fe/(Fe+Mg) ratios at the M1,M2,M3 and M13 (M1+M3) sites determined by Rietveld refinements (o), Rietveld refinements reduced by 20 % (since overestimate the Fe content) (□) and ^{57}Fe NGR data (◊). The straight lines represent the 1:1 correlation [05D1]; (**b**) the same ratios in the M4 site versus bulk Fe/(Fe+Mg) ratio (= x_{Fe} in the M1,2,3 sites) from [05D1] (solid symbols) and from [87S1] – S and [98E1, 02G1] (open symbols). Dashed isotherms were calculated from ΔG^0 (1073 K) = 20 kJ, while the solid isotherms were obtained with ΔG^0(298 K) = 62 kJ and ΔS^0 (298 K) of 54 J/K [05D1].

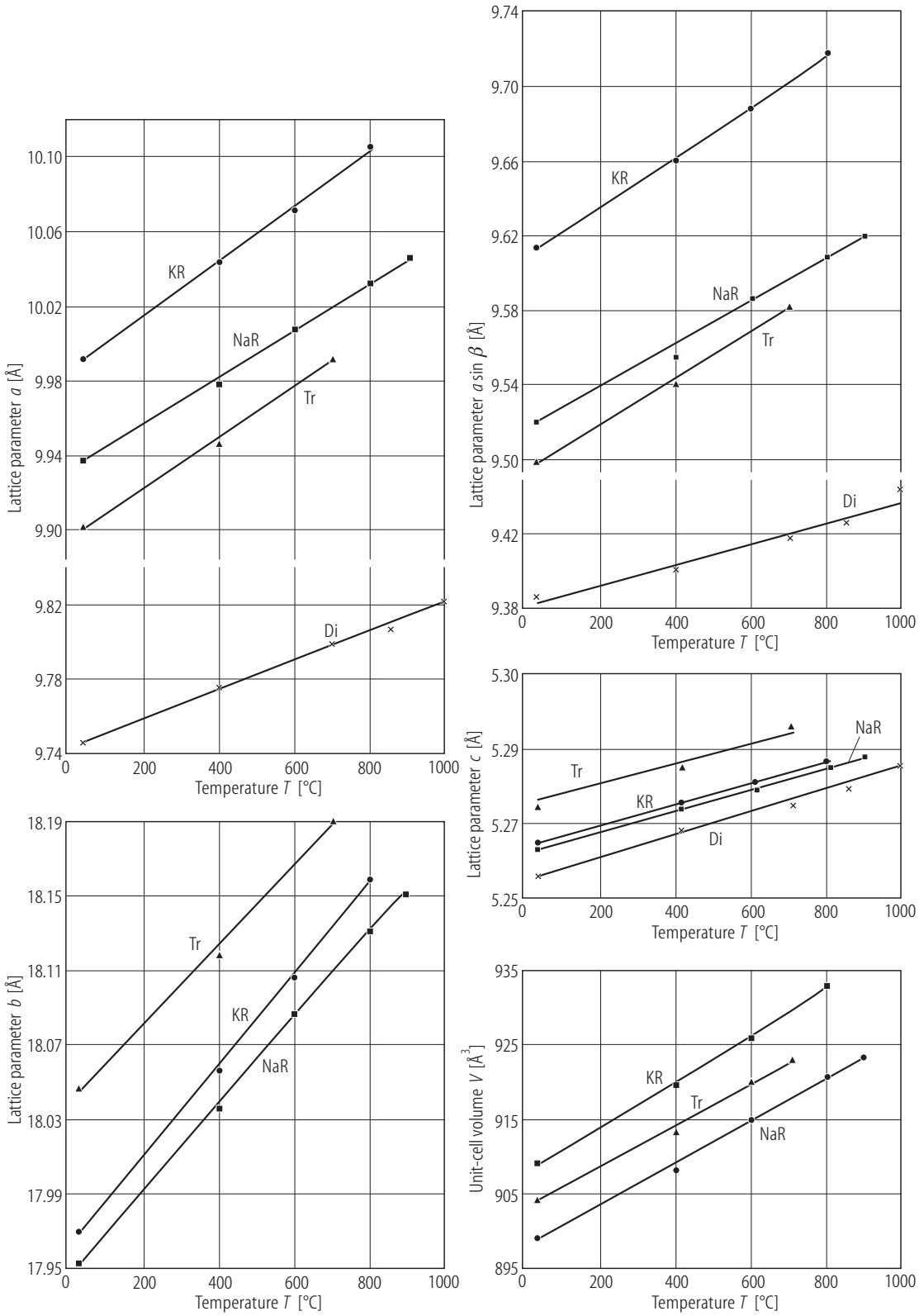

Fig. 13. Na richterite (NaR), K richterite (KR), tremolite (Tr) [83C1], diopside (Di) [79C1]. Temperature dependences of lattice parameters. I-centered cell parameters of the amphiboles are plotted.

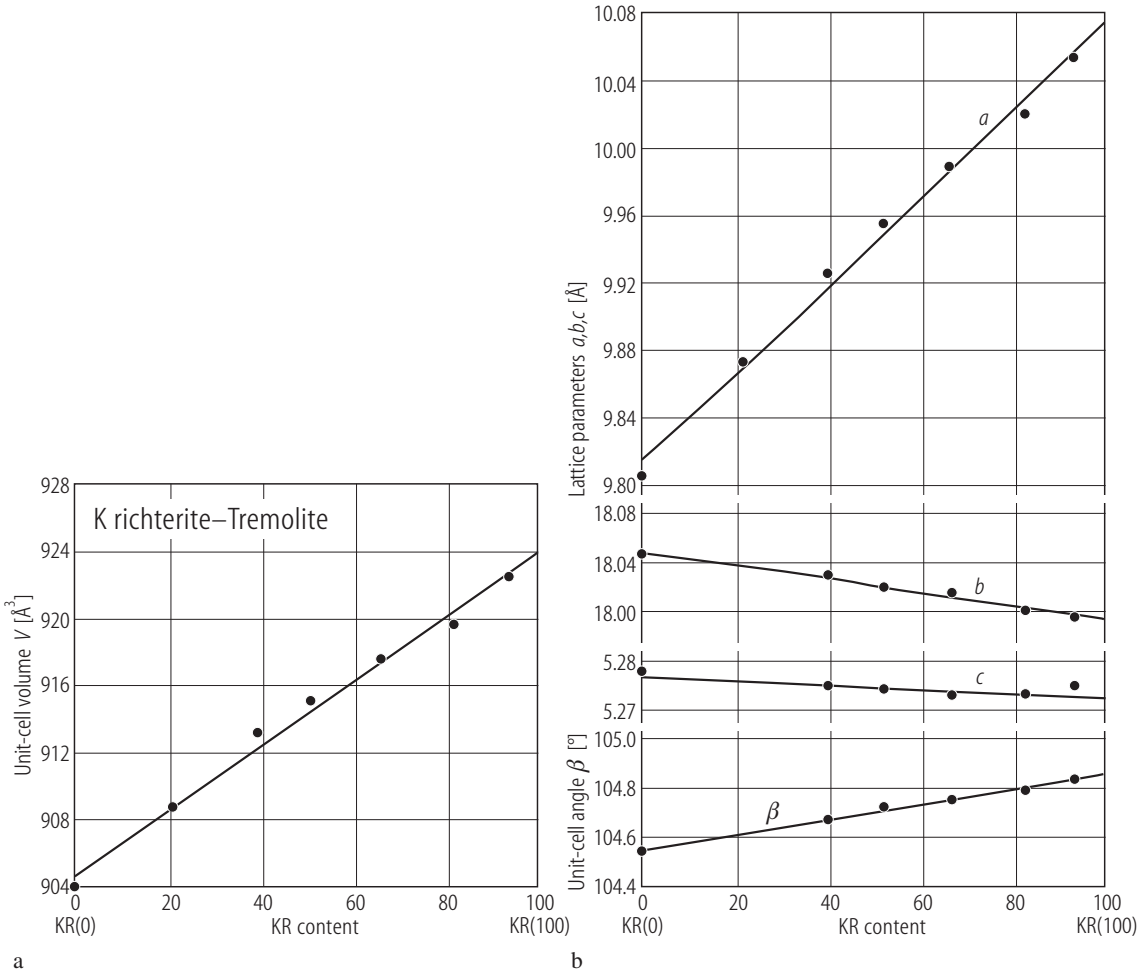

Fig. 14. K richterite – tremolite. Composition dependences of the unit-cell volume (**a**) and lattice parameters (**b**) [97H1].

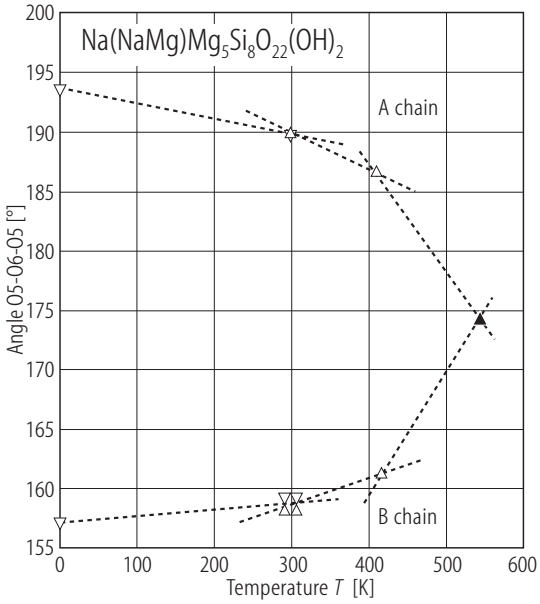

For Fig. 15 see next page

Fig. 16. $Na(NaMg)Mg_5Si_8O_{22}(OH)_2$. Change in the O5-O6-O5 angles between 8 and 573 K ∇-[05I1]; Δ-[03C1]; ▲-after $P2_1/m$ – C2/m transition [05I1]. The dotted lines are drawn as guide for the eye.

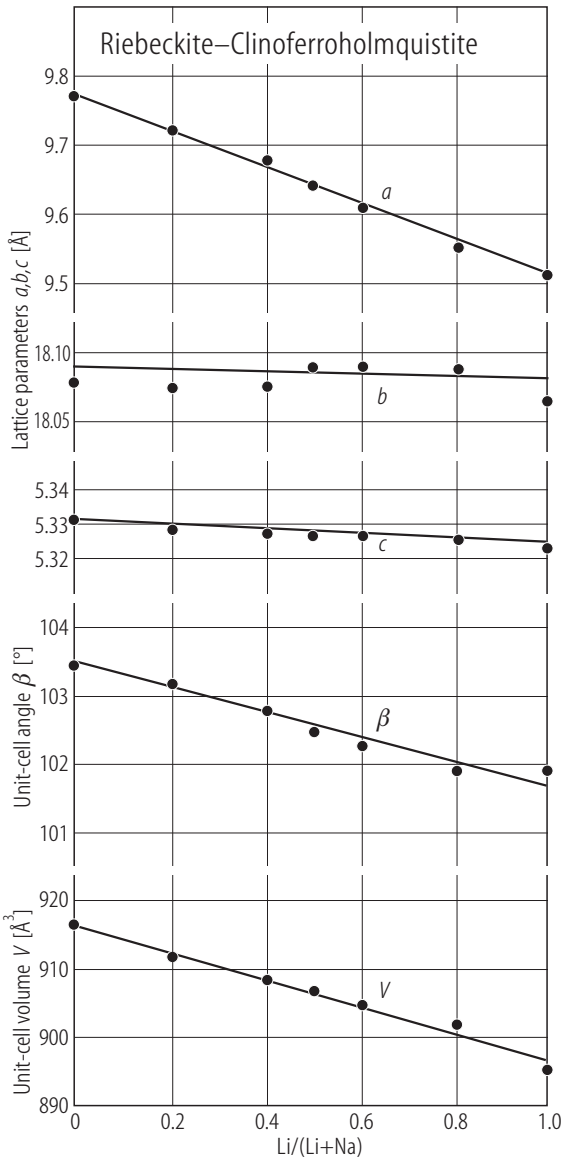

Fig. 15. Riebeckite – ferri-clinoferroholmquistite. Composition dependences of the lattice parameters [03I2].

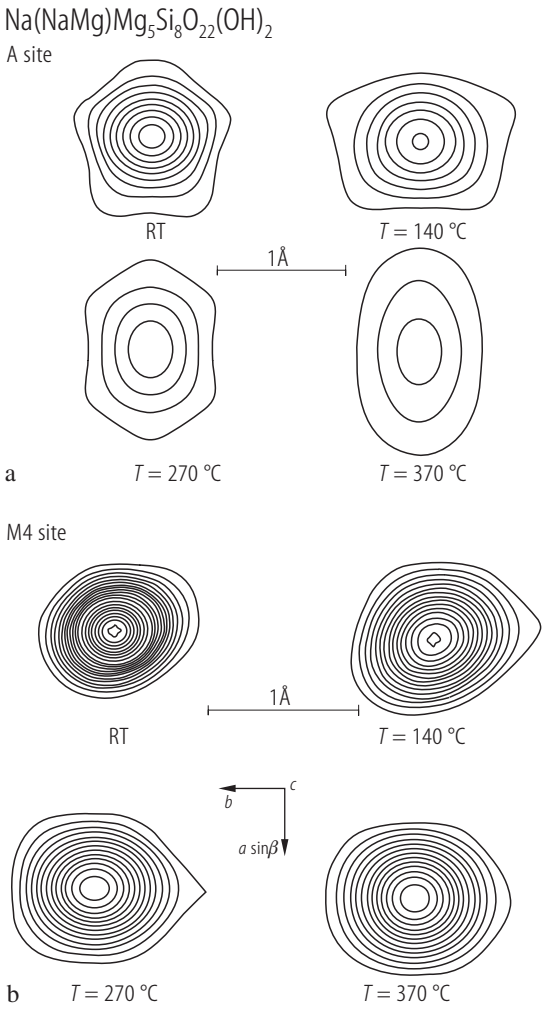

Fig. 17. $Na(NaMg)Mg_5Si_8O_{22}(OH)_2$. The shape of the electron densities (**a**) at the A site in the two symmetries; projection onto (–210), *b*-edge on the abscissa; (**b**) at the M4 site in two symmetries. Contour lines each 2 eÅ^{-3}; first line at 2 eÅ^{-3} [03C1].

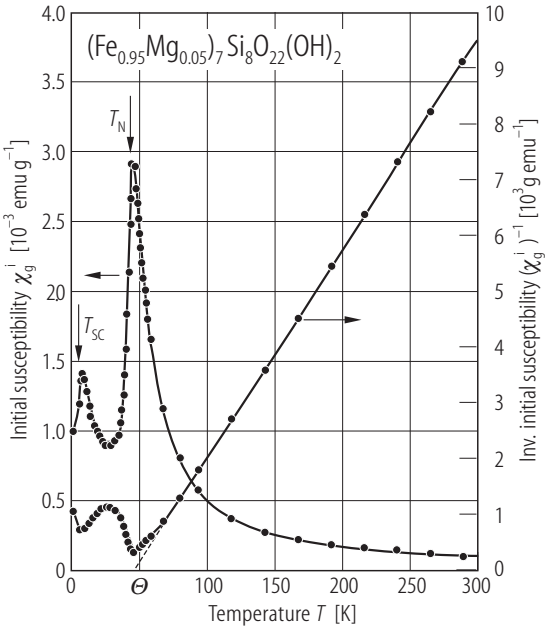

Fig. 18. $(Fe_xMg_{1-x})_7Si_8O_{22}(OH)_2$ grunerite with x = 0.95. Thermal variations of initial and inverse susceptibilities [88L1]. T_{SC}: spin canting temperature (see text).

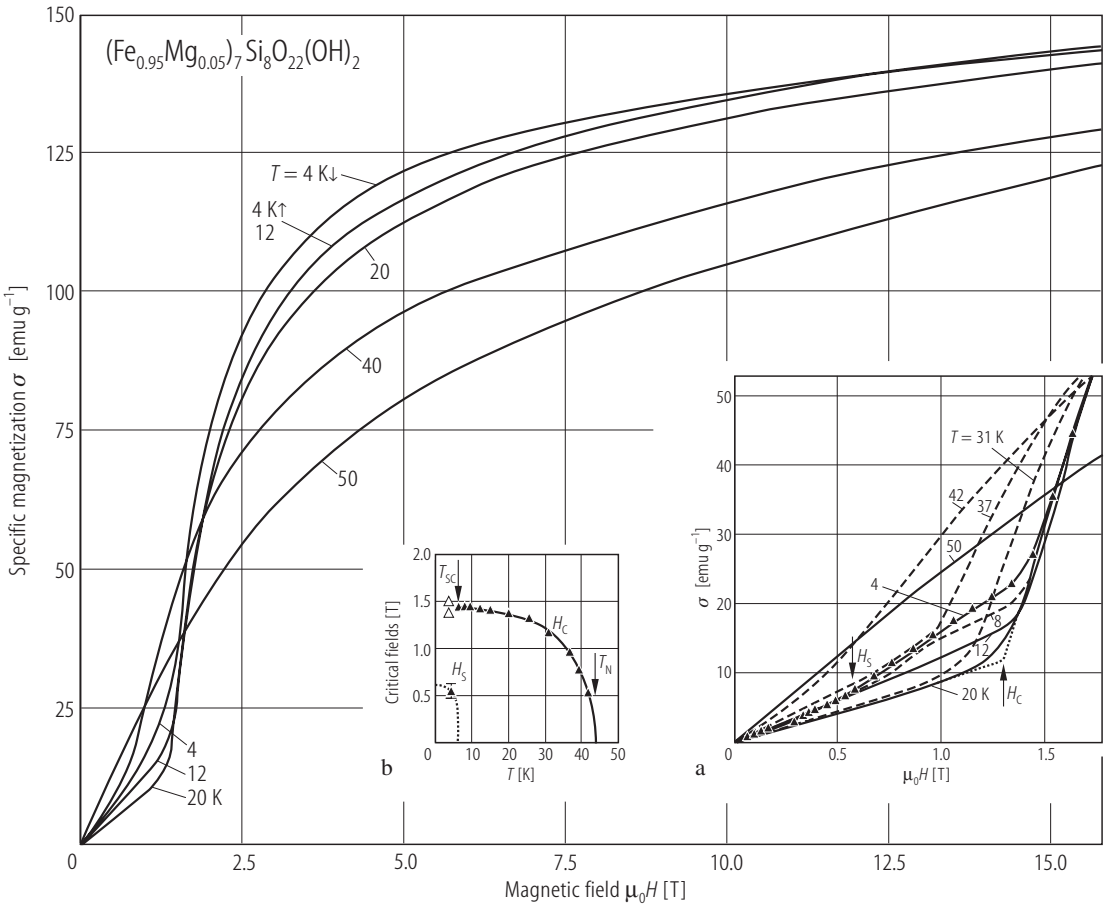

Fig. 19. $(Fe_xMg_{1-x})_7Si_8O_{22}(OH)_2$ grunerite with x = 0.95. Magnetization isotherms. Inset (a) shows details of the magnetization curves and inset (**b**) the variation with temperature of the critical threshold fields H_c and H_s (see text). The values noted on curves are T in K [88L1].

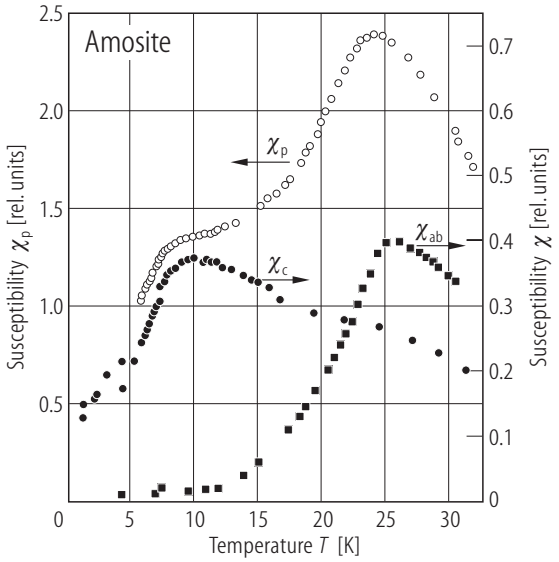

Fig. 20. Natural anthophyllite (amosite). Temperature dependence of the magnetic susceptibilities in a field of $\mu_o H = 2$ T (χ_c – parallel and χ_{ab} – perpendicular to the fibre axis and χ_p for the powdered sample) [75E1].

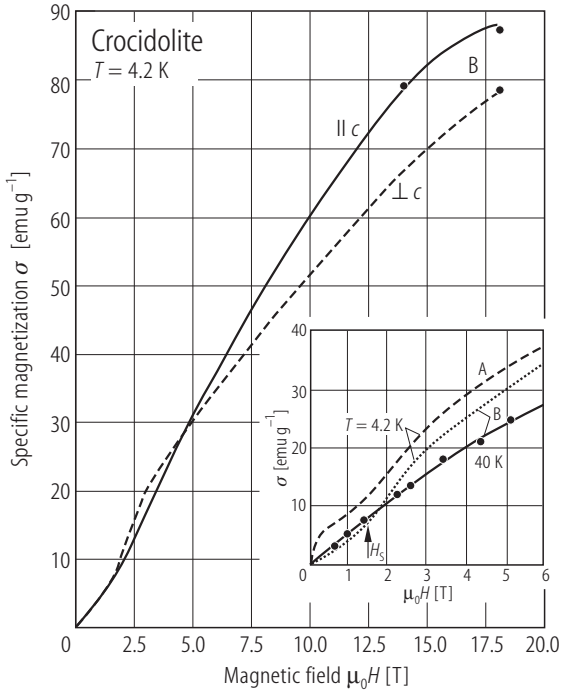

Fig. 22. Crocidolites (riebeckites A[7] and B[8]). Specific magnetization isotherms. Data in high fields were obtained on oriented fibres [83M3]. Composition in Table 6.

For Fig. 23 see next page

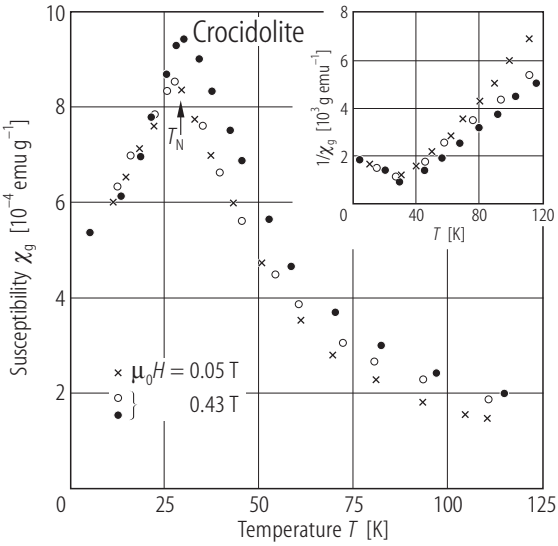

Fig. 21. Crocidolite (riebeckite)[8]. Susceptibilities and inverse susceptibilities (inset). Measurements were made with the field applied parallel (•) and perpendicular (o) to the fibre axes and for a randomly oriented sample (×) [83M3]. Composition in Table 6.

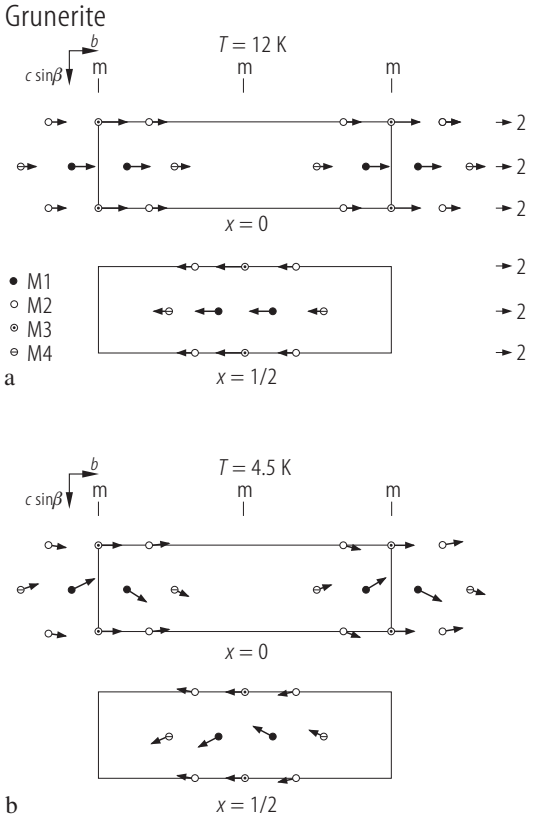

Fig. 24. Grunerite. Projection of magnetic structure perpendicular to the ***a***-axis. Arrows represent direction of the magnetic moments at (**a**) 12 K and (**b**) at 4.5 K [87G1].

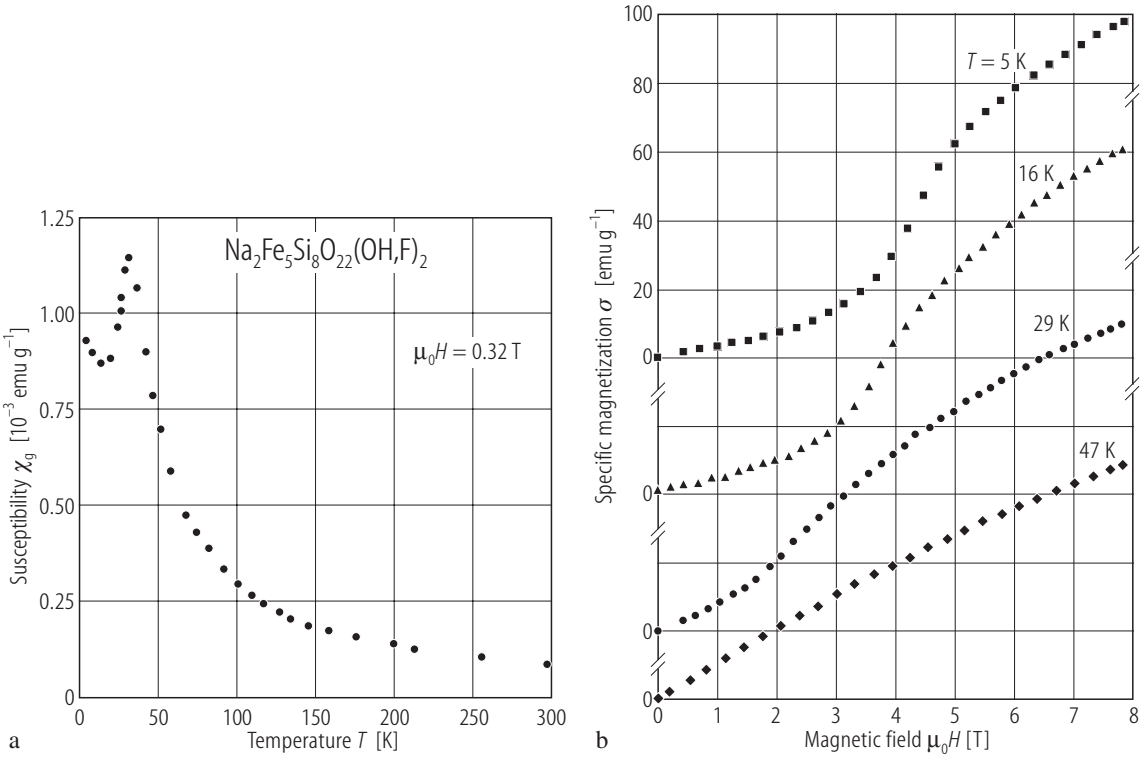

Fig. 23. $Na_2Fe_5Si_8O_{22}(OH,F)_2$. (**a**) Temperature dependence of the susceptibility in a field μ_oH = 0.32 T for a powdered sample, (**b**) specific magnetization isotherms for a single crystal in a field $\boldsymbol{H}$ || [001] [75B3].

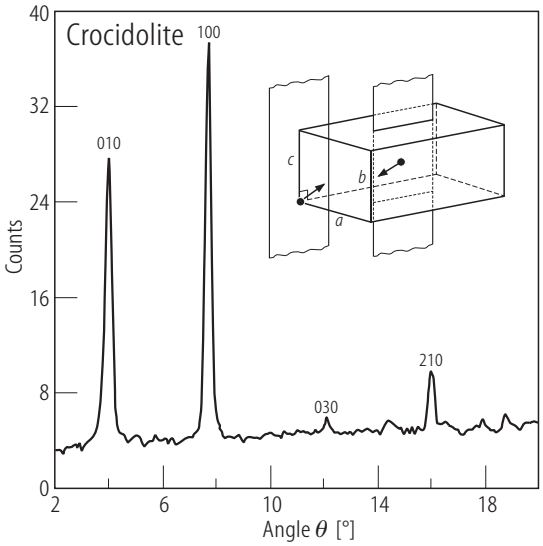

Fig. 25. Crocidolite (riebeckite). Magnetic neutron scattering pattern obtained by subtracting the diffraction pattern recorded at 40 K from that at 5 K. The magnetic structure is shown in the insert [83M3].

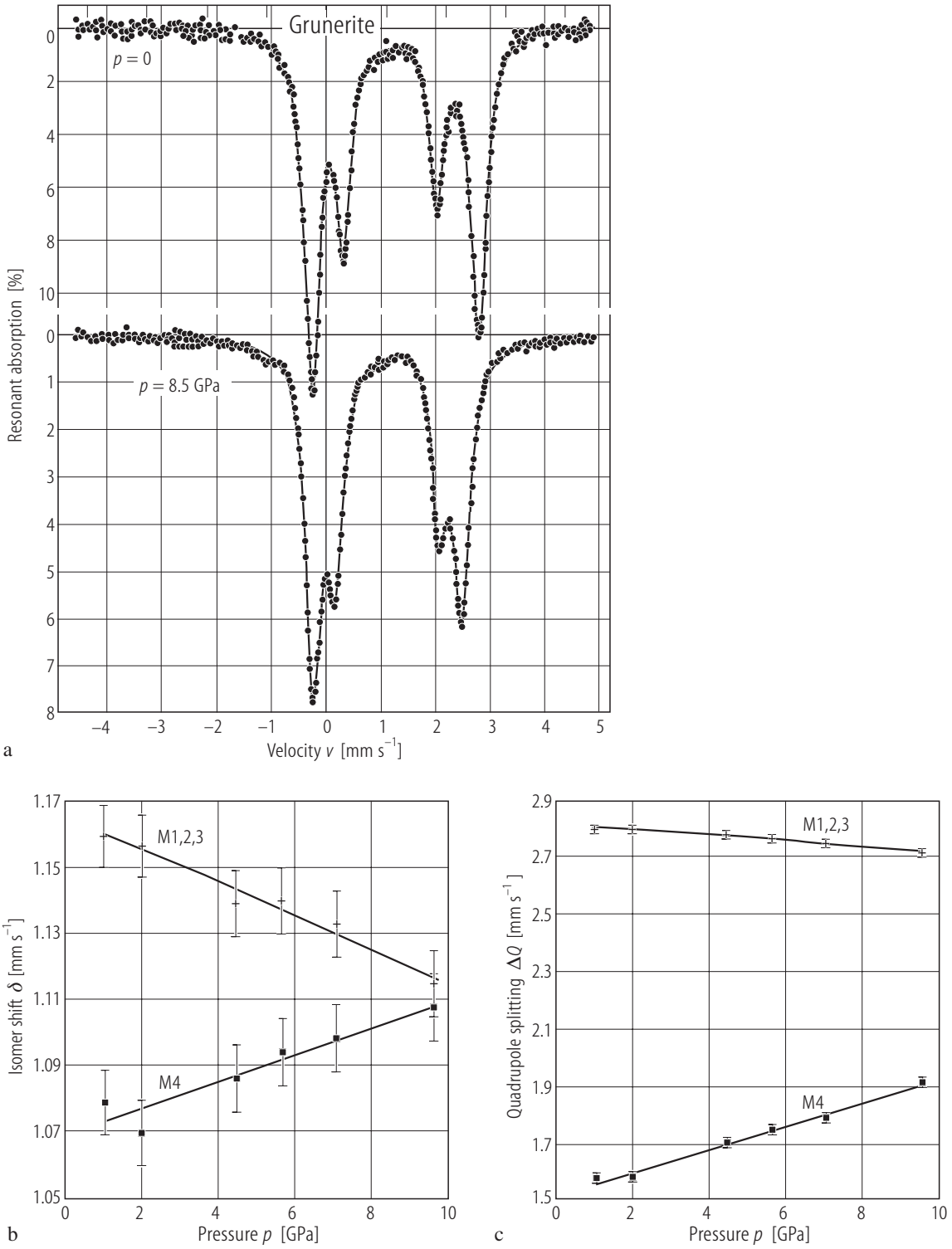

Fig. 26. Grunerite[5]. ^{57}Fe NGR spectra at ambient pressure and 8.5 GPa (**a**). Pressure dependences of the isomer shifts (**b**) and quadrupole splittings (**c**) [92Z1]. Composition in Table 8.

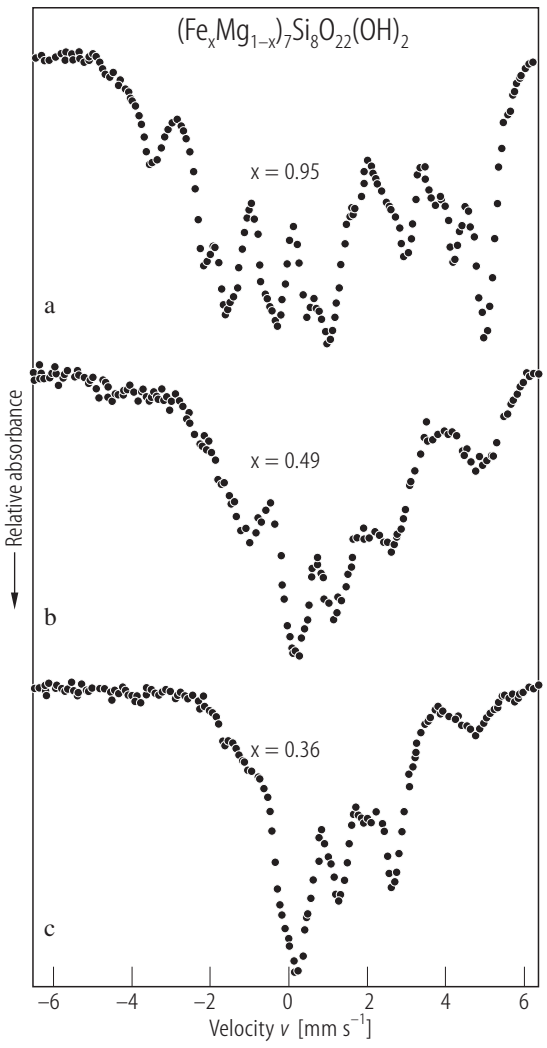

←
Fig. 27. $(Fe_xMg_{1-x})_7Si_8O_{22}(OH)_2$. ^{57}Fe NGR spectra at (**a**) 14 K (x = 0.95), (**b**) 4.2 K (x = 0.49) and (**c**) 1.6 K (x = 0.36) [88L1].

Fig. 28. Cummingtonite. Temperature dependences of the quadrupole splittings, ΔQ for (**a**) Fe^{2+} at the (M1,M2,M3) sites, (**b**) Fe^{2+} at M4 site [02B1]. Open symbols (C2/m structure), filled symbols ($P2_1/m$ structure). ↓

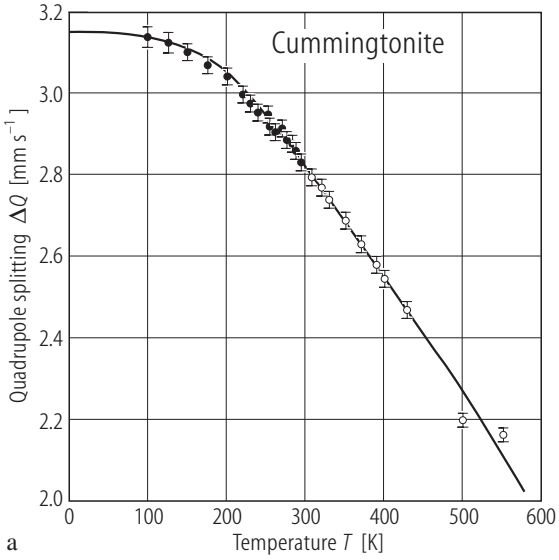

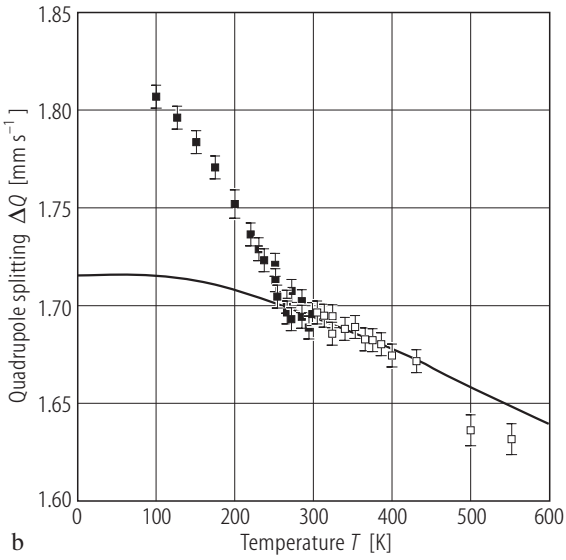

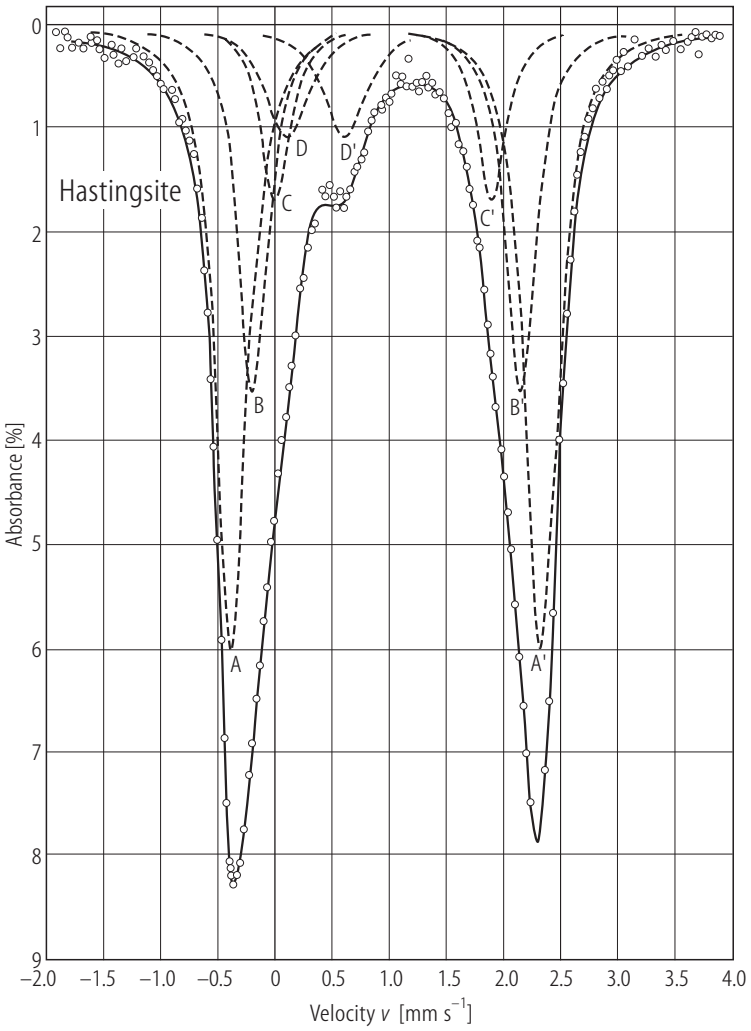

Fig. 29. Hastingsite (synthetic). ^{57}Fe NGR spectrum at room temperature. Doublets AA', BB', CC' are assigned to Fe^{2+} and doublet DD' to Fe^{3+}, all in octahedral coordination [82T1].

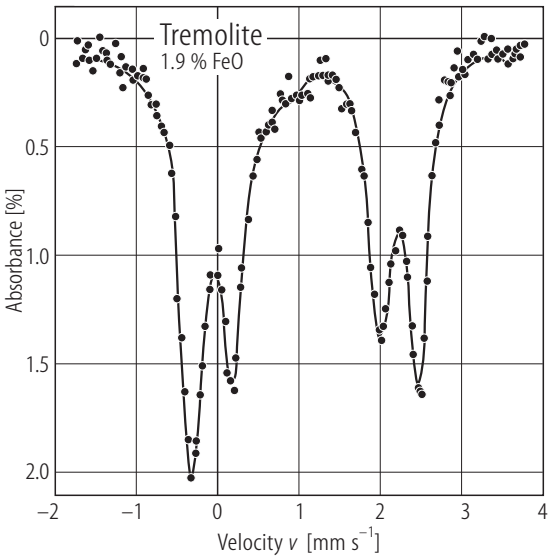

Fig. 30. Tremolite. ^{57}Fe NGR spectrum at room temperature [79G1].

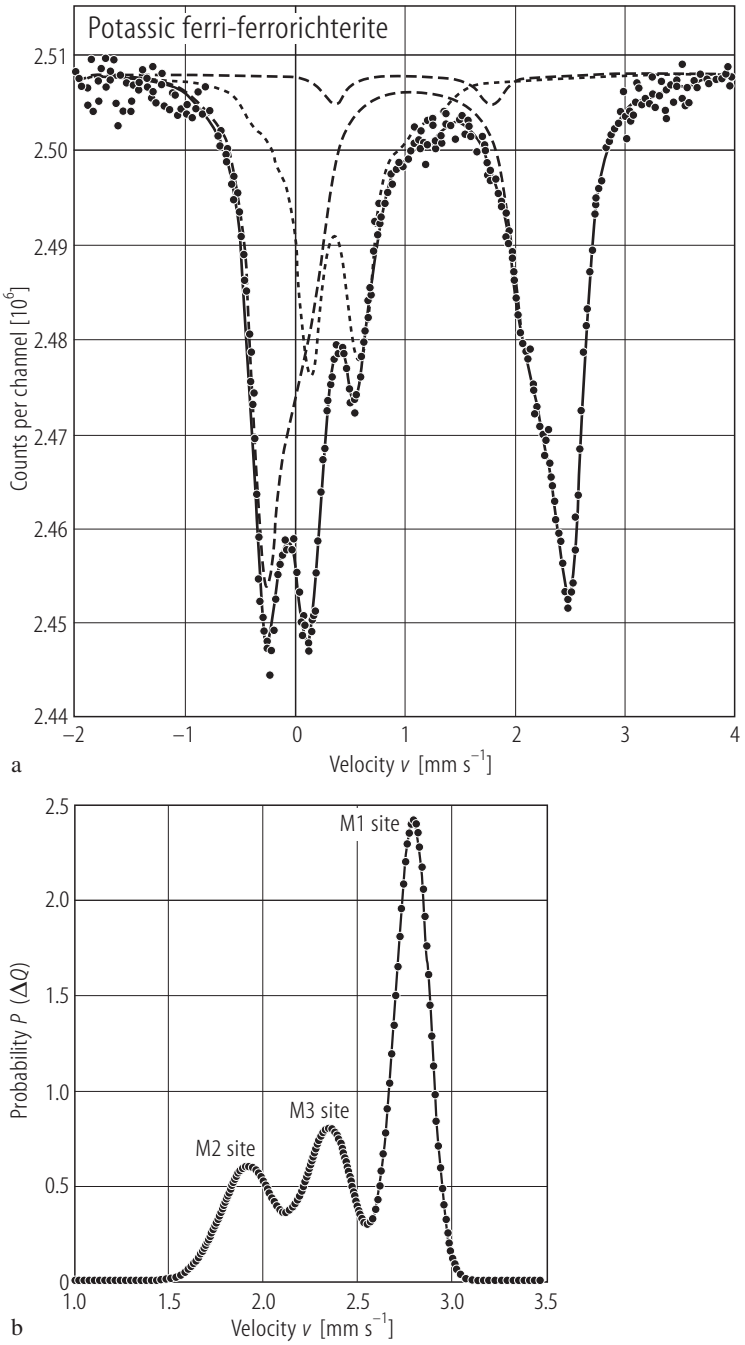

Fig. 31. Potassic ferri-ferrorichterite[40]. (**a**) ^{57}Fe NGR spectrum at 298 K and (**b**) the corresponding trimodal $\Delta Q(Fe^{2+})$ distribution curve [02R2]. Composition in Table 8.

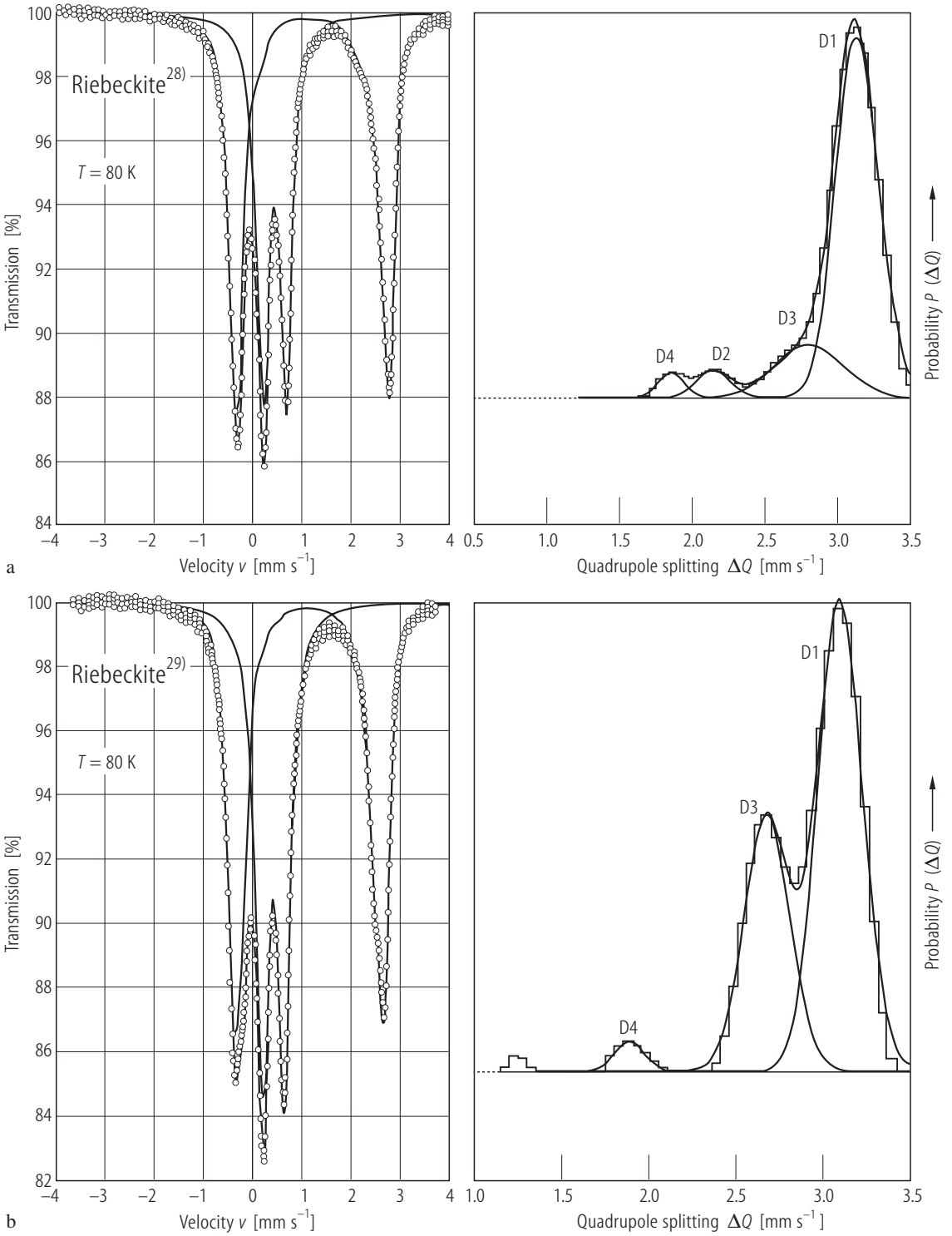

Fig. 32. Riebeckite[28)] (**a**) and riebeckite[29] (**b**). ^{57}Fe NGR spectra at 80 K. The spectra have been fitted with a superposition of a ferric doublet and a ferrous quadrupole splitting distribution (full lines). The calculated probability distribution, $P(\Delta Q)$, is reproduced in the right part of the drawing [96V1]. Composition in Table 8.

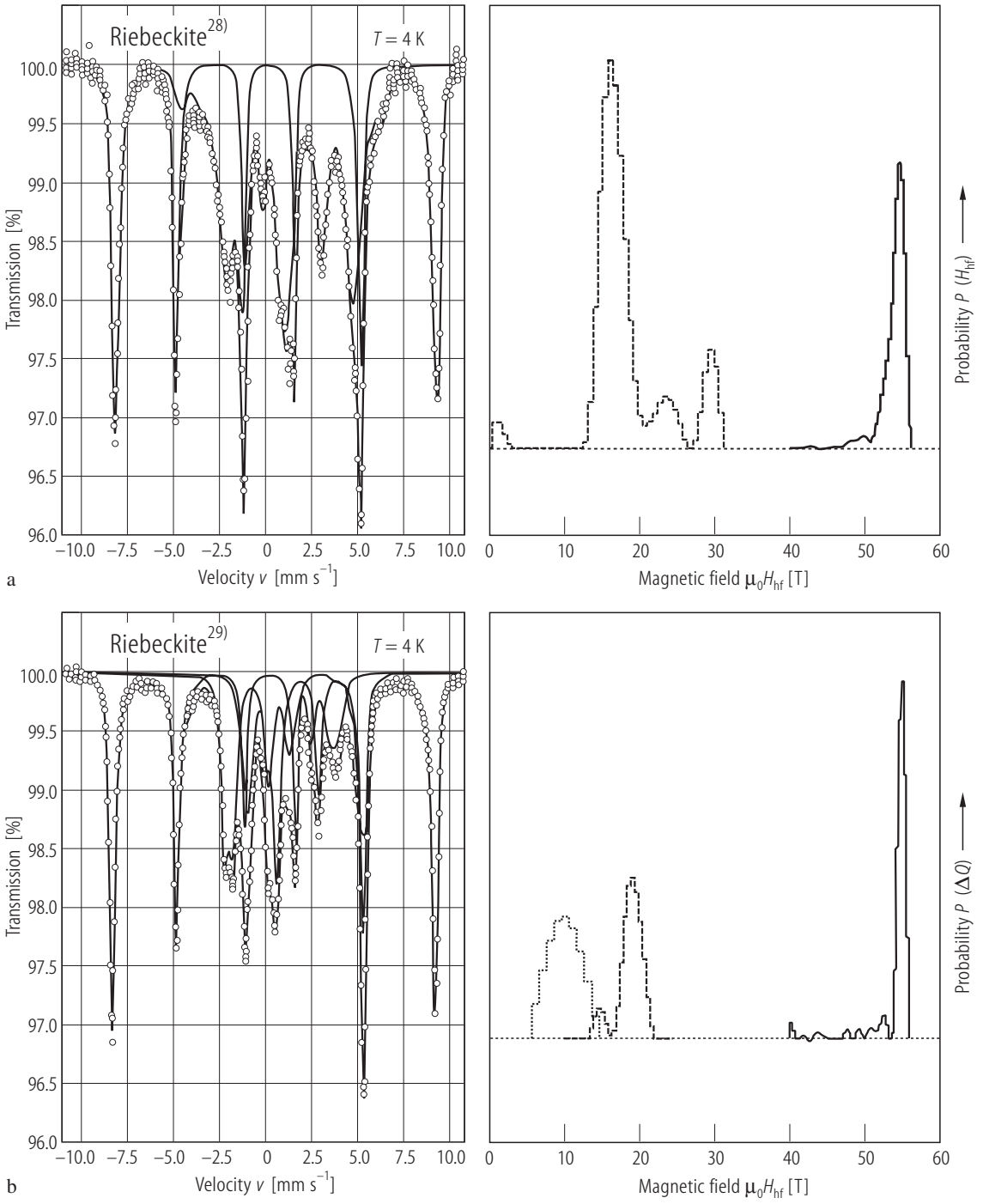

Fig. 33. Riebeckite[28)] (**a**) and riebeckite[29)] (**b**). ^{57}Fe NGR spectra at 4 K fitted with a superposition of one ferric and one ferrous hyperfine-field distribution. The distribution profiles are shown on right side in full line for the ferric component and dashed line for the ferrous one (**a**), while in (**b**) the distribution profiles in dashed are for the Fe^{2+}(M1) component and in dotted line for the Fe^{2+} (M3) component (full line as in (**a**) [96V1]. Composition in Table 8.

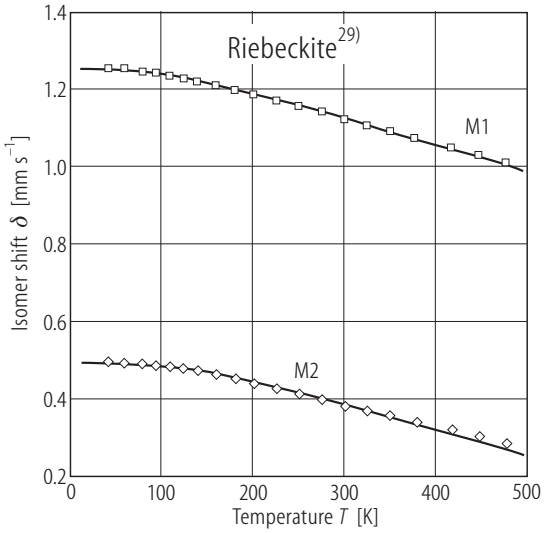

Fig. 34. Riebeckite[29)]. Calculated (full line) and experimental isomer shifts as function of temperature for M1(Fe^{2+}) and M2(Fe^{3+}) [96V1]. Composition in Table 8.

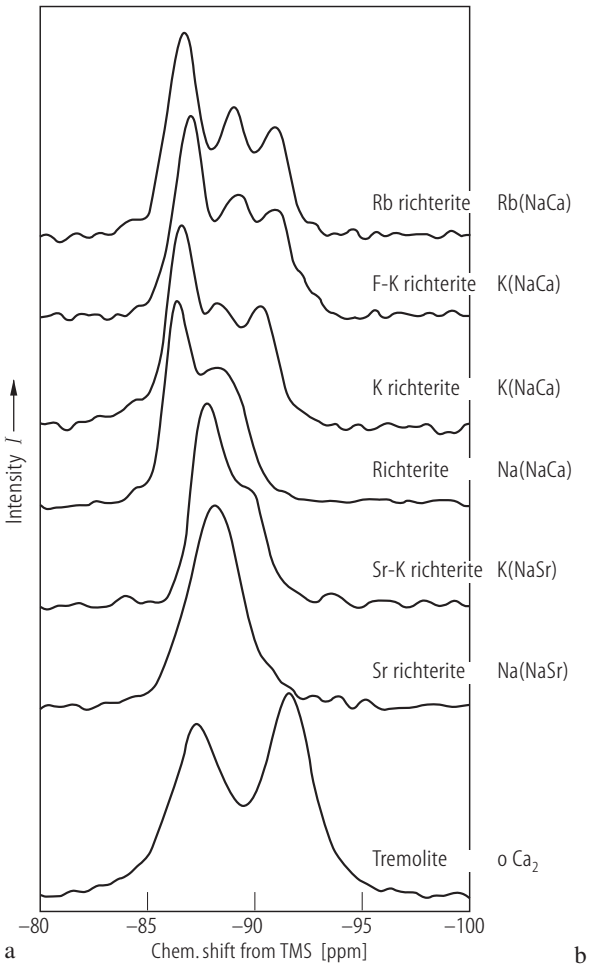

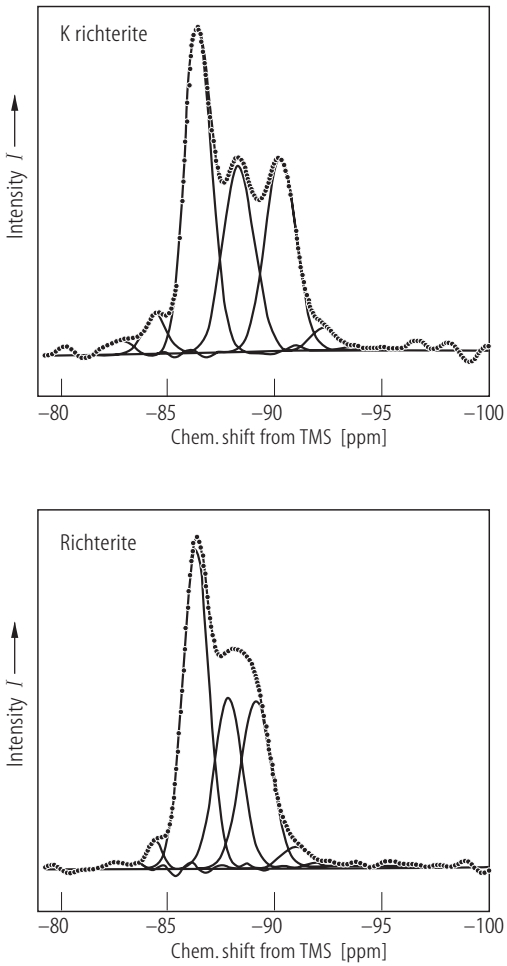

Fig. 35. Synthetic richterites and natural tremolite. (**a**) ^{29}Si MAS NMR spectra. The small peak at –84 ppm in some spectra is the only peak that does not cross-polarize and is due to a very small amount of clinopyroxene impurity. The A site and M4 chemistries are indicated in right part. (**b**) Simulations of the ^{29}Si MAS NMR spectra of potassium richterite and richterite using a pure Gaussian peak shape. The dots are experimental data [98W1].

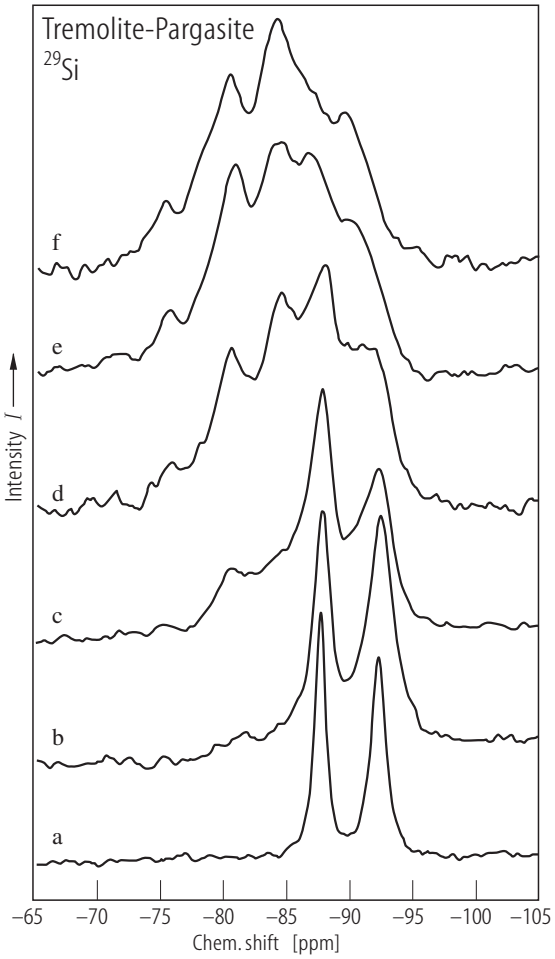

Fig. 36.
$Ca_2Mg_5Si_8O_{22}F_2$ (curve *a*); $Na_{0.2}Ca_2Mg_{4.8}Ga_{0.6}Si_{7.6}O_{22}F_2$ (*b*); $Na_{0.4}Ca_2Mg_{4.6}Ga_{1.2}Si_{7.2}O_{22}F_2$ (*c*); $Na_{0.6}Ca_2Mg_{4.4}Ga_{1.8}Si_{6.8}O_{22}F_2$ (*d*); $Na_{0.8}Ca_2Mg_{4.2}Ga_{2.4}Si_{6.4}O_{22}F_2$ (*e*); $NaCa_2Mg_4Ga_3Si_6O_{22}F_2$ (*f*). ^{29}Si MAS NMR spectra of $^{[4]}Si$ [99S2].

For Fig. 37 see next page

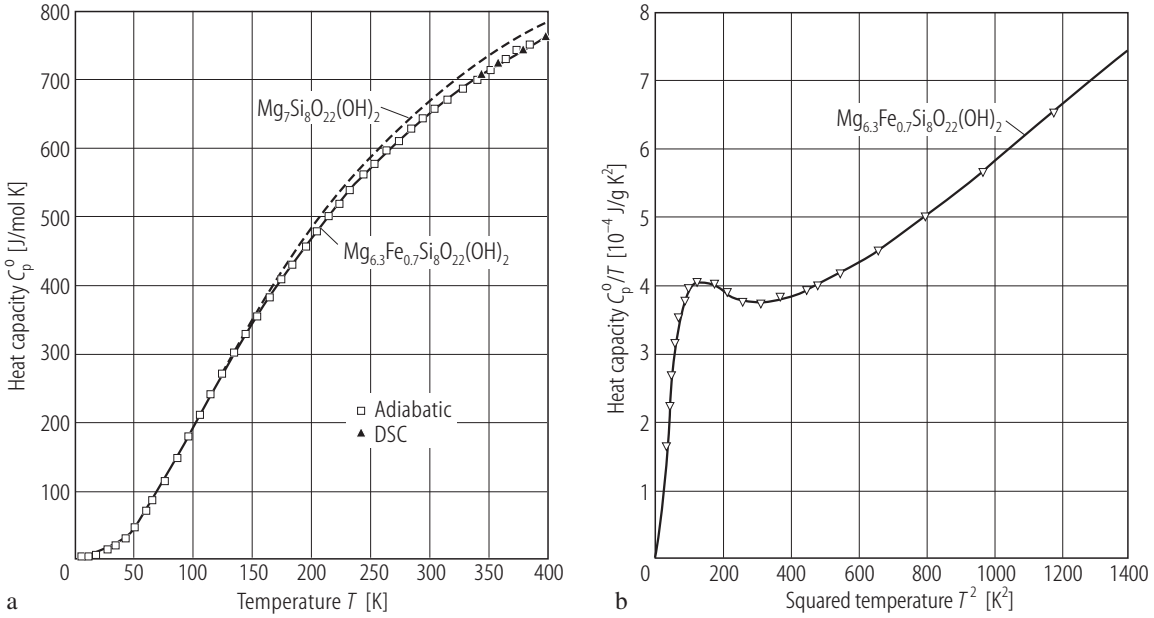

Fig. 38. $Mg_{6.3}Fe_{0.7}Si_8O_{22}(OH)_2$, $Mg_7Si_8O_{22}(OH)_2$. Temperature dependence of the heat capacity (**a**) and C_p/T vs. T^2 at low temperature (**b**) [85K1, 85K2].

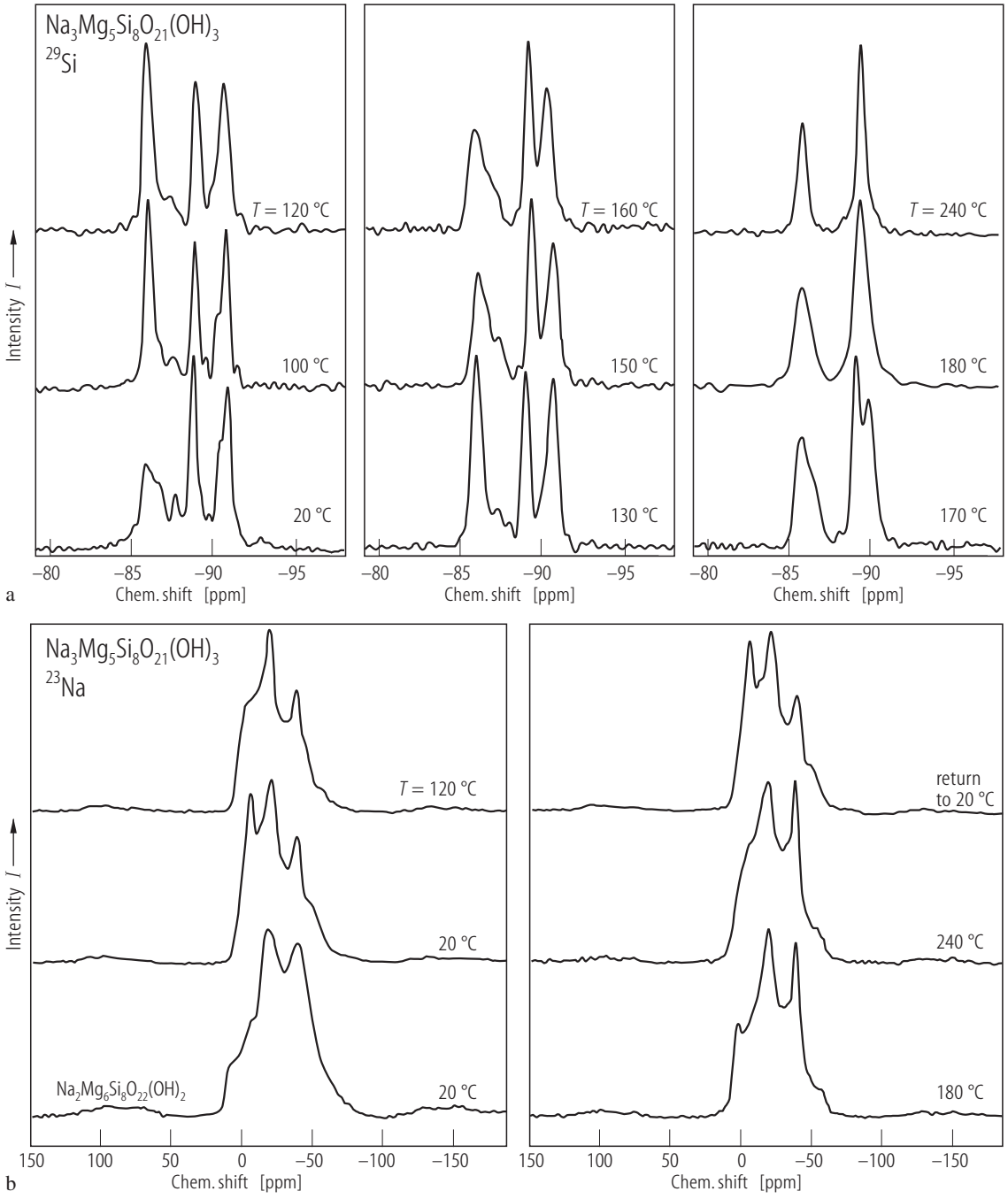

Fig. 37. $Na_3Mg_5Si_8O_{21}(OH)_3$. (**a**) ^{29}Si and (**b**) ^{23}Na MAS NMR spectra as function of temperature. In (**b**) is also shown the spectrum of $Na_2Mg_6Si_8O_{22}(OH)_2$ at 20°C [96L1].

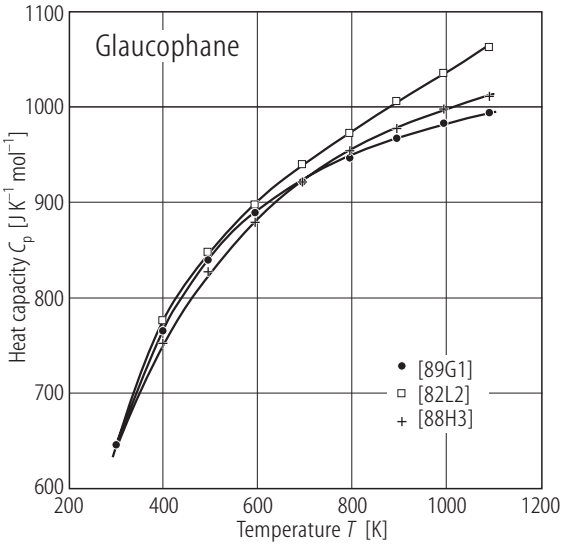

Fig. 39. $Na_{0.01}(Na_{1.93}Ca_{0.05}Fe_{0.02})$-$(Mg_{2.60}Fe^{2+}_{0.41}Fe^{3+}_{0.15}Cr_{0.01}Al_{1.83})(Si_{7.92}Al_{0.08})O_{22}(OH)_2$ glaucophane. Heat capacity (corrected for composition) vs. temperature [89G1]. The data obtained by [82L2] and [88H3] are also given.

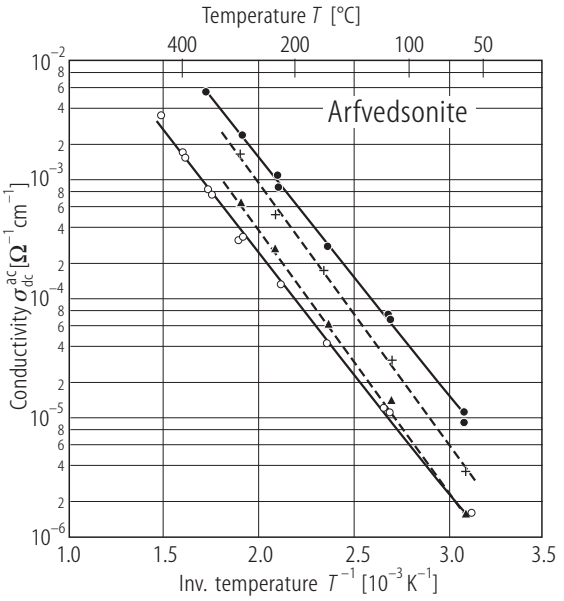

Fig. 40. Arfvedsonite. Logarithm of extrapolated conductivity for $\omega \to 0$ from impedance plots σ^{ac}_{dc} versus T^{-1}. Volume conductivity: crosses: second run; full circles: seventh run. Conductivity assumed to occur at or across internal surface layers generated by defects of variable kinds: triangles: second run; open circles: seventh run. Current in all cases parallel to [001] [96S1].

For Fig. 41 see next page

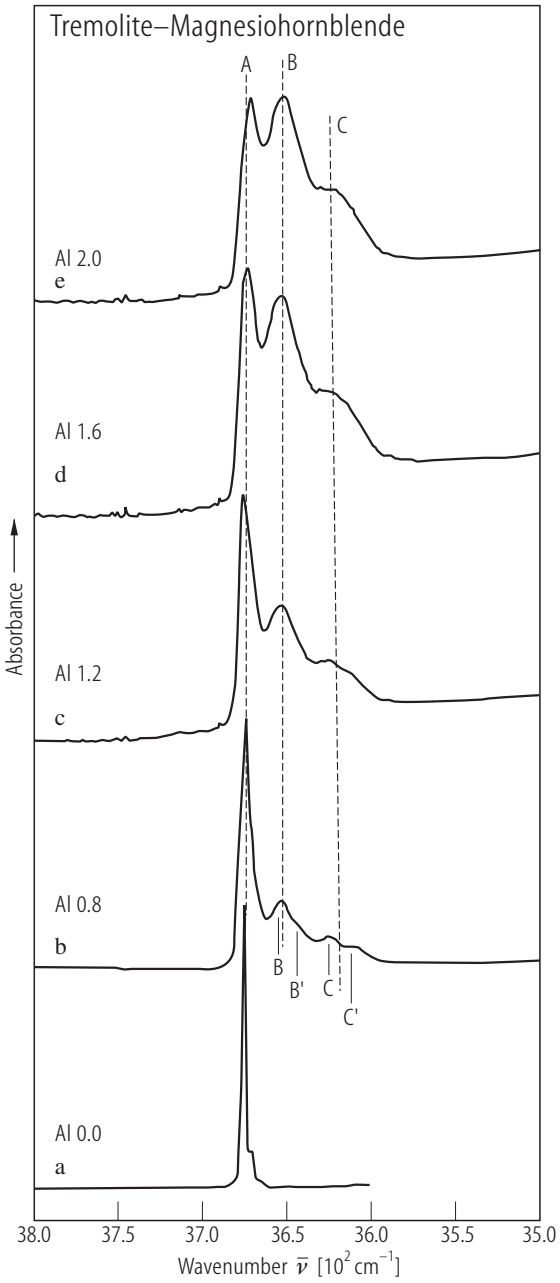

Fig. 42. $Ca_{1.8}Mg_{5.2}Si_8O_{22}(OH)_2$ – $Ca_{1.8}(Mg_{4.2}Al)(Si_7Al)O_{22}(OH)_2$. Infrared spectra in the principal OH-stretching region [00H2].

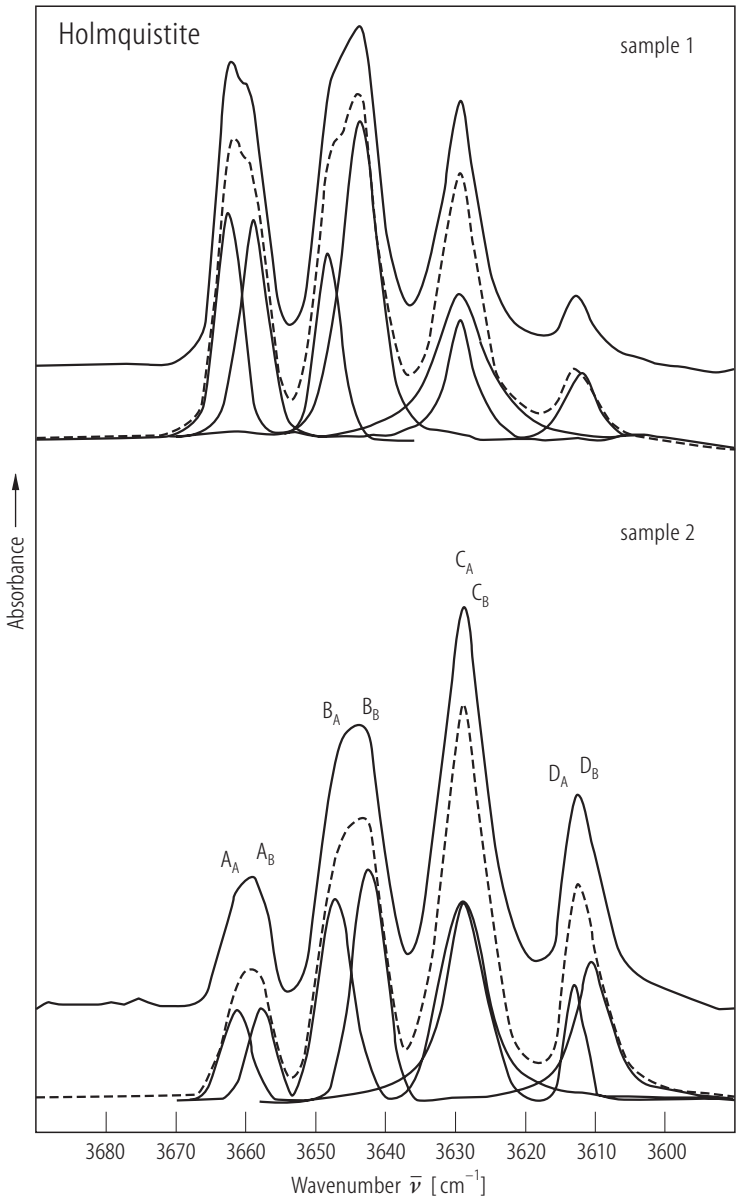

Fig. 41. Holmquistite (natural). Infrared OH-stretching spectra of two samples heat treated in air [03I3].

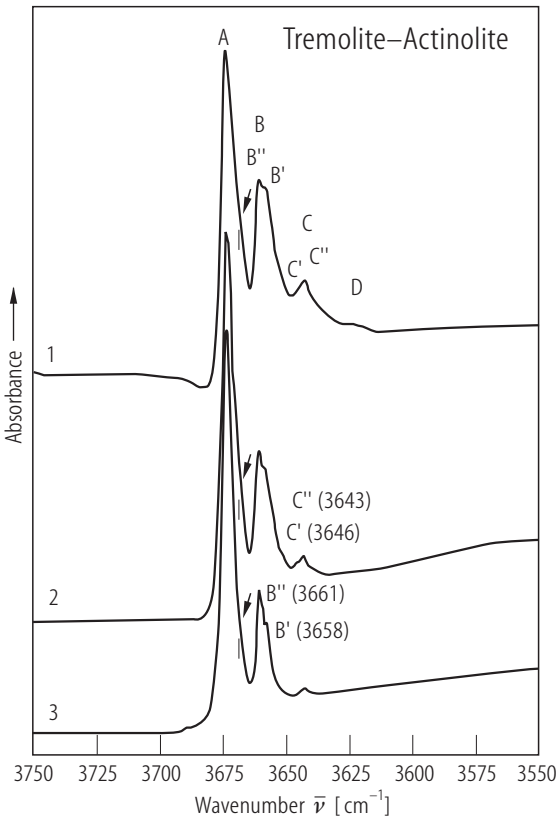

Fig. 43. Tremolite – Fe^{2+} poor actinolites. IR OH-stretching spectra [02I1].
Curve 1:
$(K_{0.010}Na_{0.150})(Ca_{1.806}Na_{0.194})(Mn_{0.007}Fe^{2+}_{0.626}Mg_{4.164}Al_{0.178})(Si_{7.905}Al_{0.095})O_{22}(OH)_2$
Curve 2:
$Na_{0.058}(Ca_{1.866}Na_{0.134})(Mn_{0.005}Fe^{3+}_{0.611}Mg_{4.221}Al_{0.134})Si_8O_{22}(OH)_2$
Curve 3:
$(K_{0.003}Na_{0.058})(Ca_{1.886}Na_{0.089}Mn_{0.025})(Fe^{2+}_{0.287}Mg_{4.749}Cr^{3+}_{0.009})(Si_{7.946}Al_{0.048})O_{22}(OH)_2$

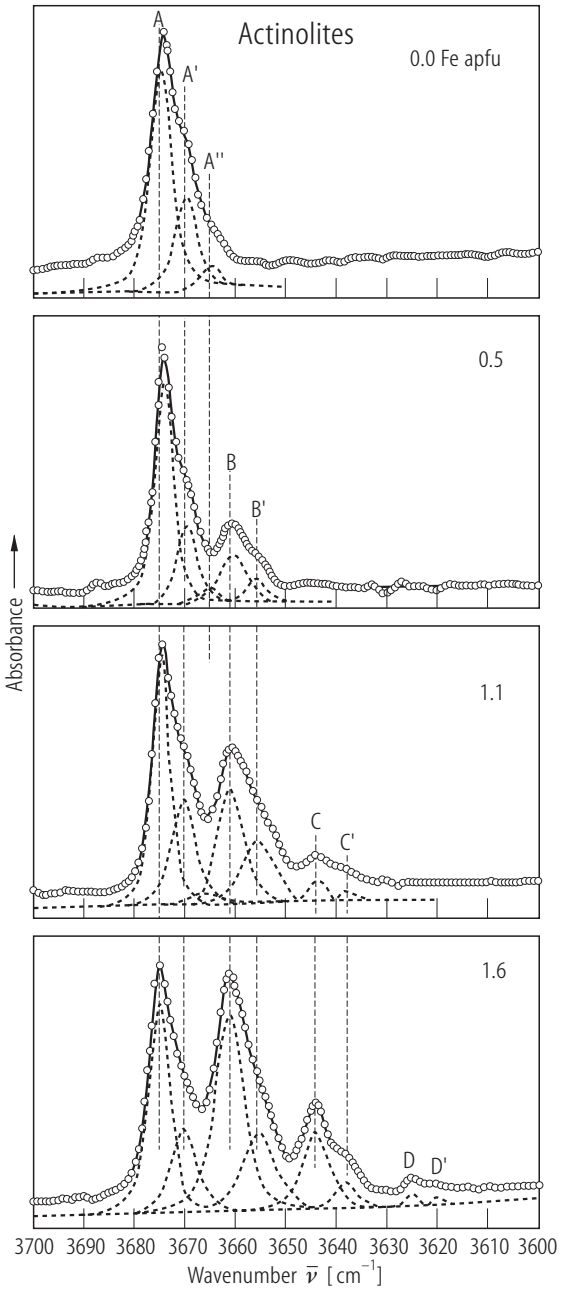

Fig. 44. Low calcium actinolites. FTIR spectra. Parameter: Fe content. The solid curves are the calculated fit to the observed data (circles) and dashed curves are the individual bands fitted to the spectra [05D1].

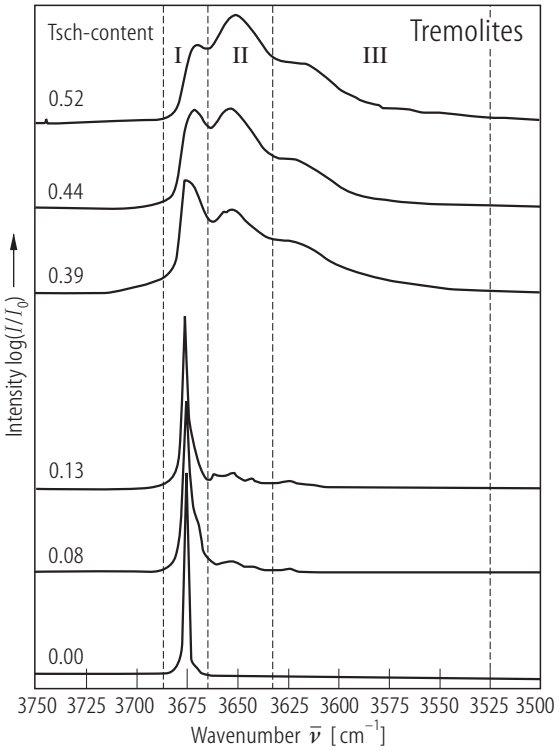

Fig. 45. Aluminium tremolites. FTIR spectra of the OH-stretching vibration [03N1]. Tsch: tschermakite.

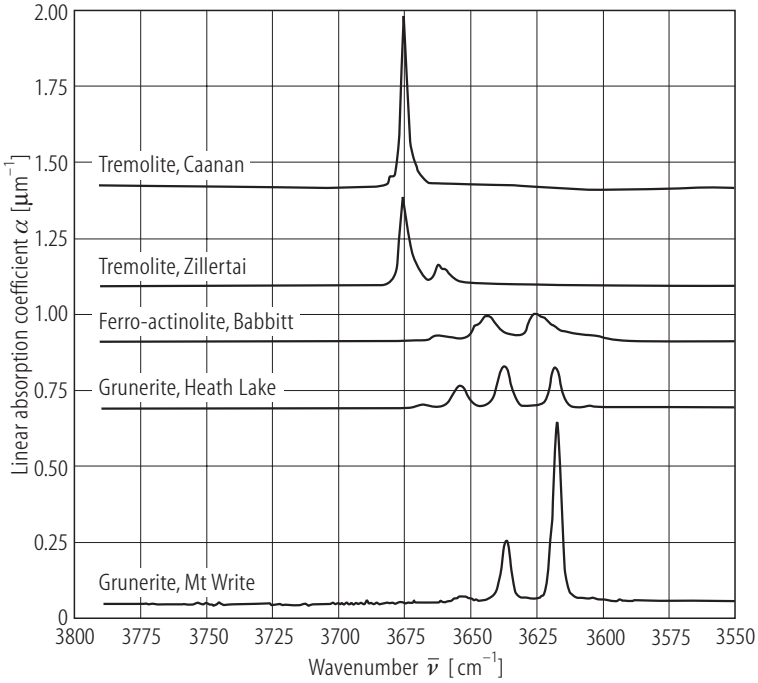

Fig. 46. Natural Ca and Fe-Mg amphiboles. IR spectra obtained on (010) sections polarized in the α-direction [91S1].

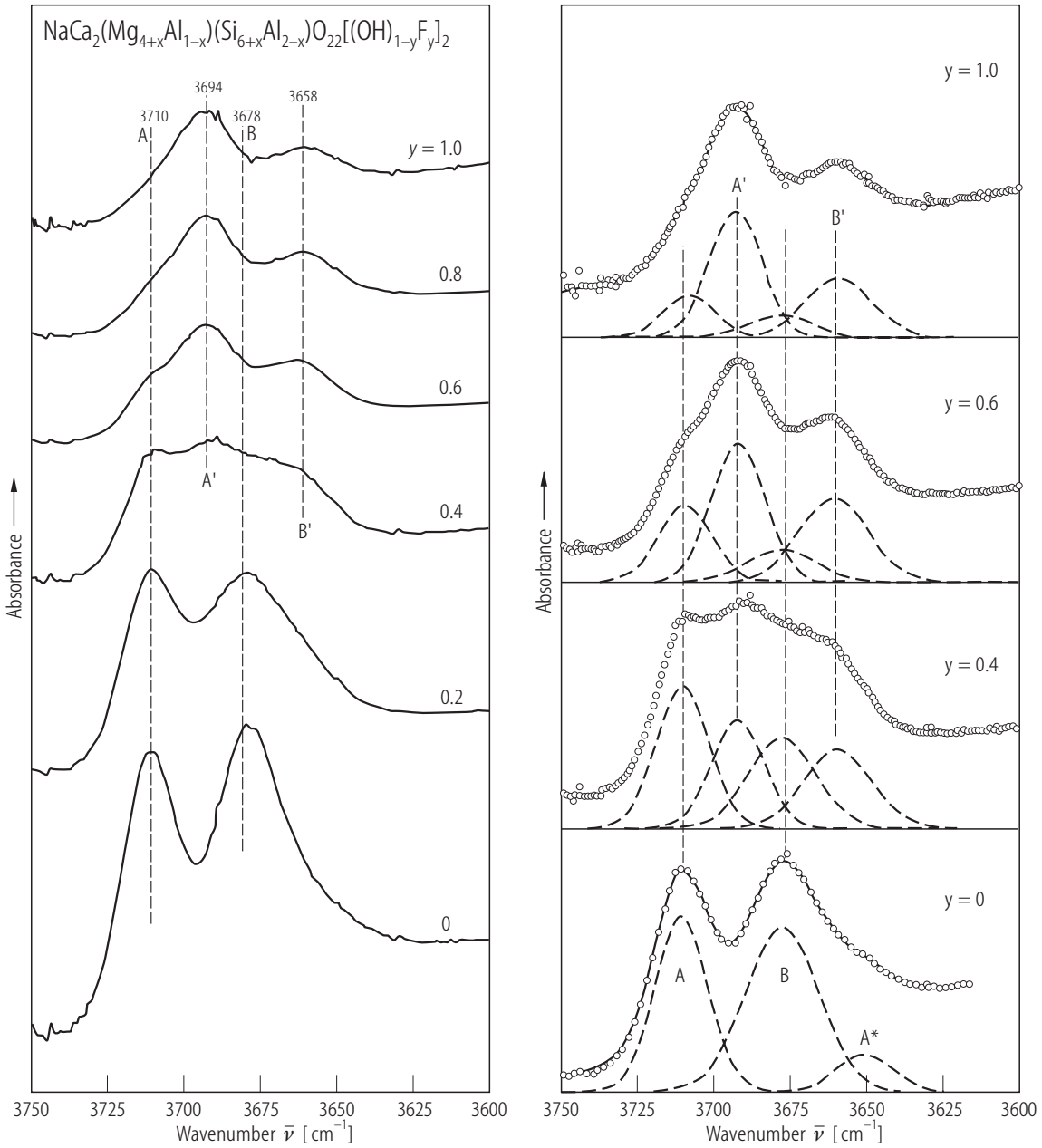

Fig. 47. Pargasites $NaCa_2(Mg_{4+x}Al_{1-x})(Si_{6+x}Al_{2-x})O_{22}[(OH)_{1-y}F_y]_2$. FTIR spectra in the OH-stretching region for different F content (y) [00R1]. Right part shows spectra of left part resolved into symmetric Gaussian bands.

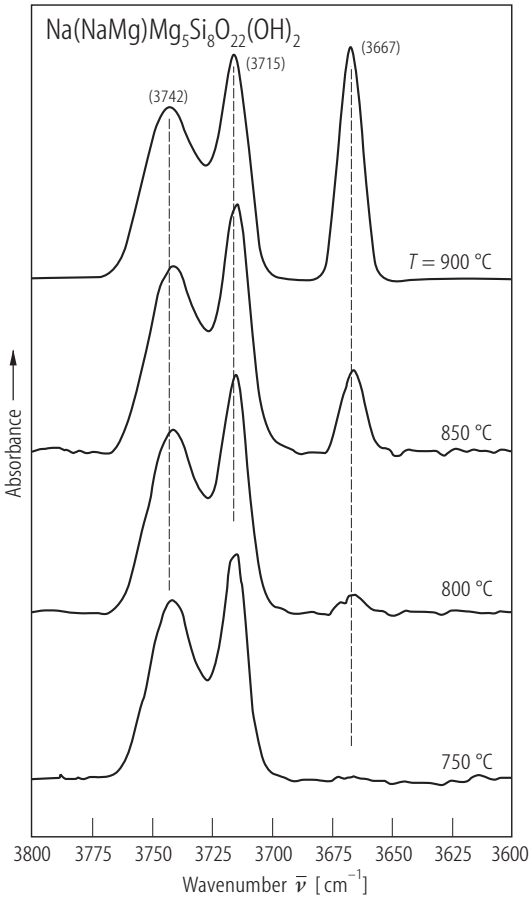

Fig. 48. $Na(NaMg)Mg_5Si_8O_{22}(OH)_2$. FTIR spectra in the OH-stretching region for samples with different synthesis temperatures [04I1].

For Fig. 49 see next page

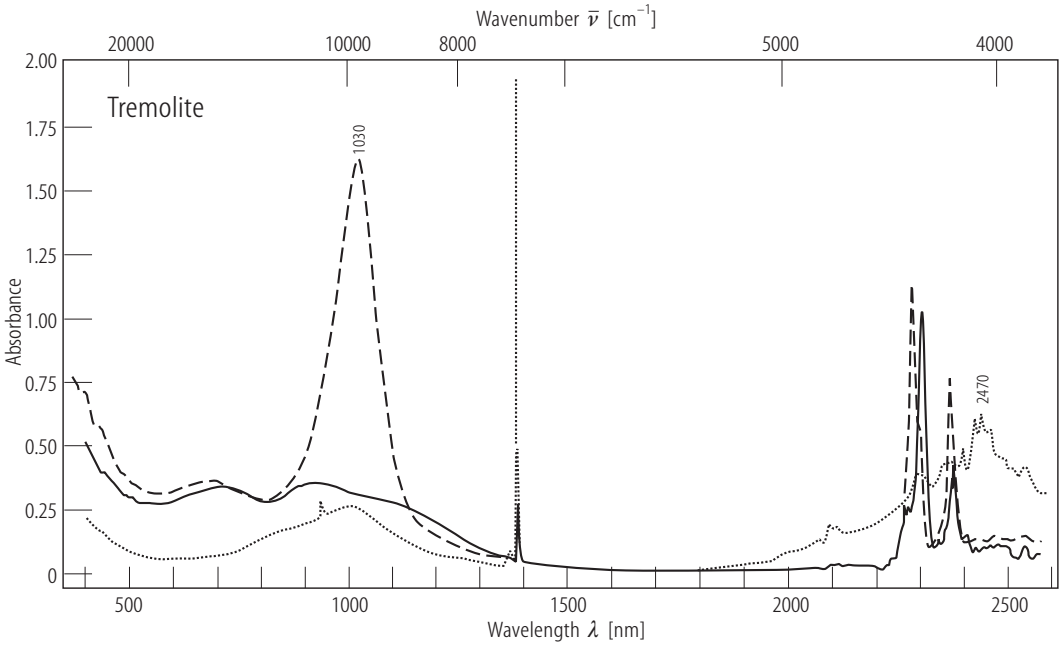

Fig. 50. Natural tremolite. Room temperatura spectra: α-spectrum (·····), β-spectrum (– – – –) and γ-spectrum (—). $\alpha \wedge c$ = 17°; crystal thickness 1.0 mm [77G1].

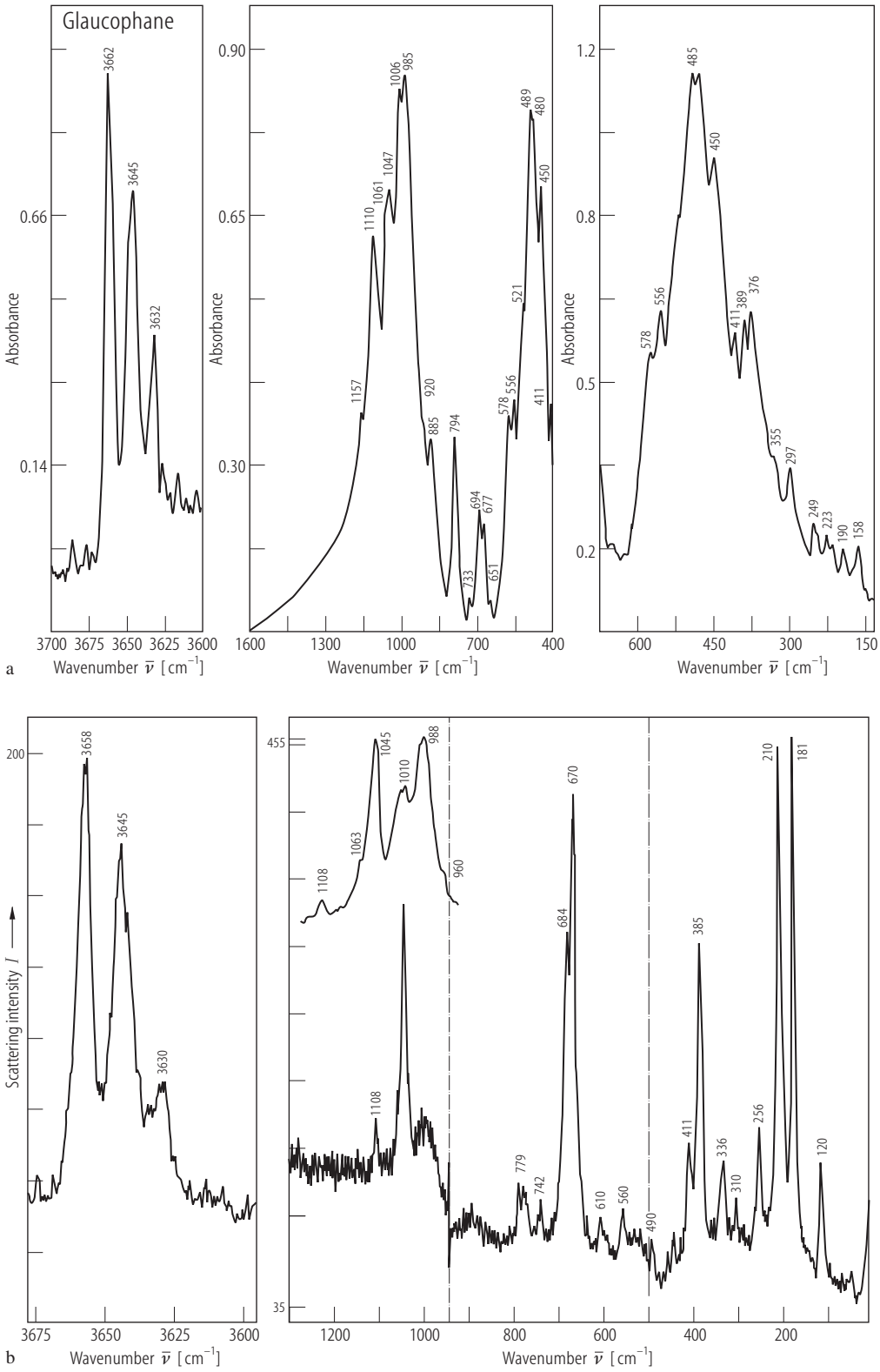

Fig. 49. Glaucophane. (**a**) Infrared spectra, (**b**) Raman spectra [89G1].

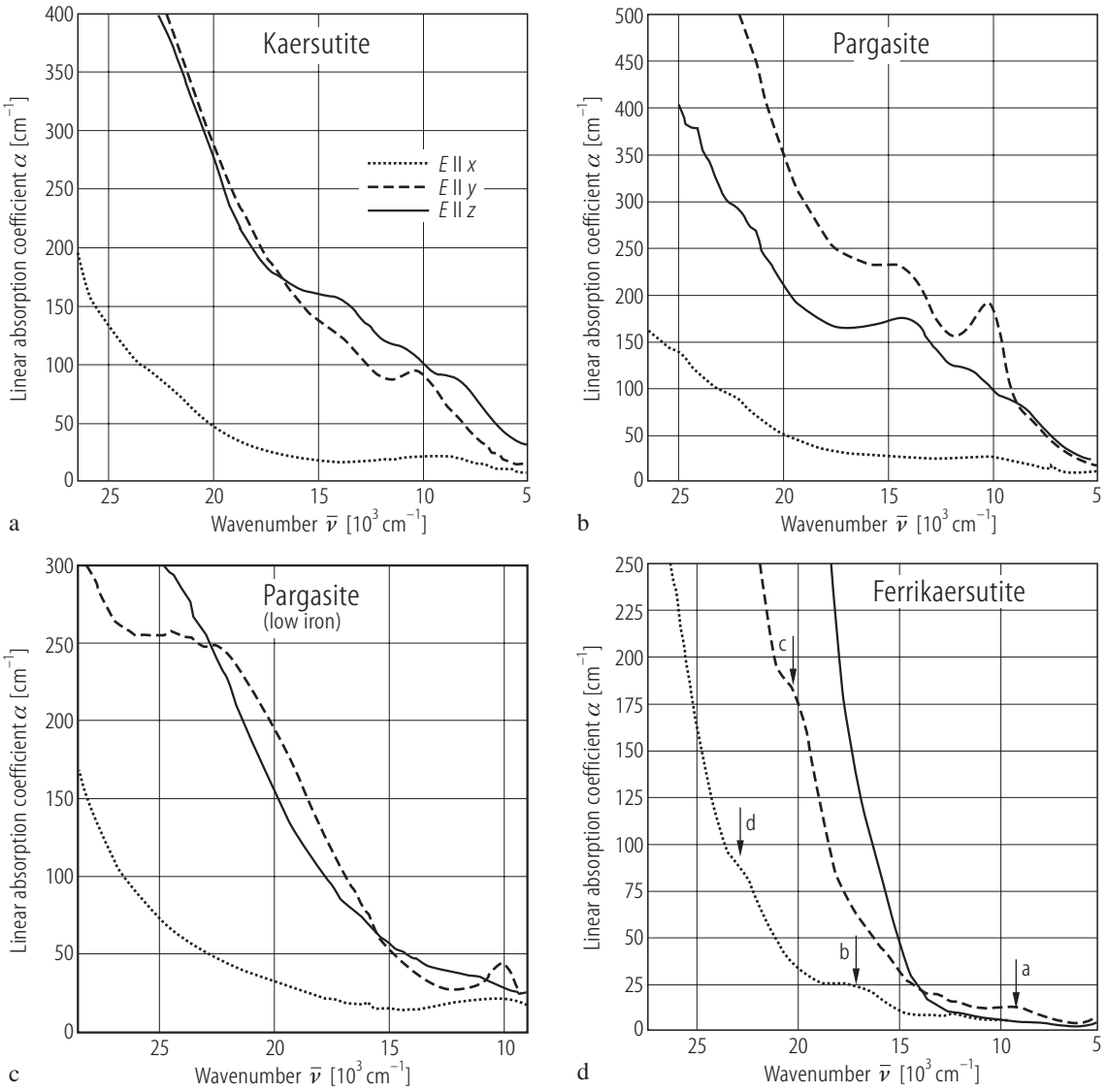

Fig. 51. Kaersutite (**a**), pargasite (**b**), low iron pargasite (**c**) and ferrikaersutite (**d**). Optical spectra [99T1].

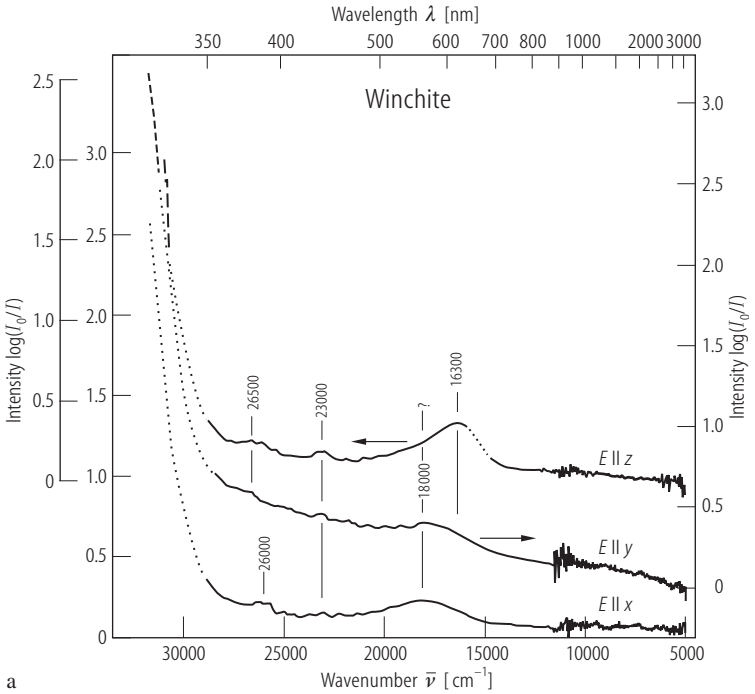

a

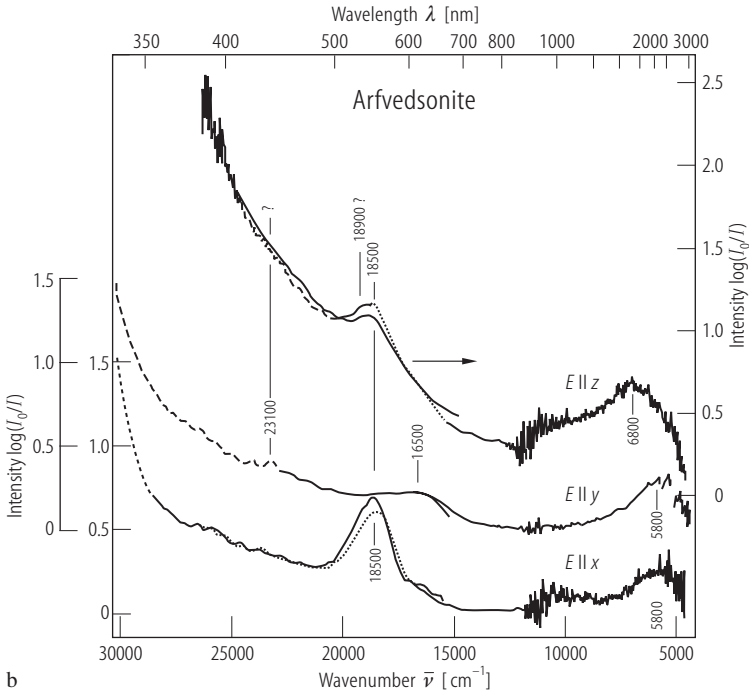

b

Fig. 52. Winchite (**a**) and arfvedsonite (juddite) (**b**). Polarized spectra at 295 K. In (**a**), spectra $\boldsymbol{E} \parallel \boldsymbol{x}$ and $\boldsymbol{z}$ were taken from a crystal slab $\perp \boldsymbol{b}$ with t = 71 µm, spectrum $\boldsymbol{E} \parallel \boldsymbol{y}$ from slab $\perp \boldsymbol{c}$ with t = 77 µm. Uncertainties are high below 12000 cm^{-1} and above 30000 cm^{-1}. In (**b**) data obtained at 110 K are shown by solid lines and those at 295 K by broken lines. Spectra $\boldsymbol{E} \parallel \boldsymbol{x}$ and $\boldsymbol{y}$ were obtained from a crystal slab $\perp \boldsymbol{b}$ with t = 75 µm, spectra $\boldsymbol{E} \parallel \boldsymbol{z}$ from slabs $\perp \boldsymbol{c}$ with t = 81 µm [86G1].

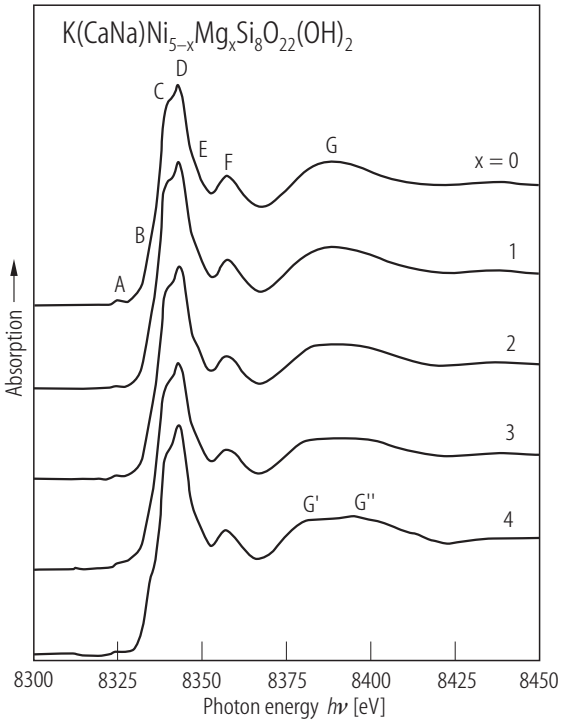

Fig. 53. $K(CaNa)Ni_{5-x}Mg_xSi_8O_{22}(OH)_2$ richterites. Ni K edge XANES spectra [00G1]. Changes as a function of the increasing Ni/Mg substitution in the join are evident in the edge region (peaks C and D) and in the energy range 8375…8400 eV (peaks G, G', G'').